Rotation-free triangular plate and shell elements

Eugenio Oñate* and Francisco Zárate

*International Centre for Numerical Methods in Engineering, Universidad Politécnica de Cataluña,
Gran Capitán s/n, 08034 Barcelona, Spain*

SUMMARY

The paper describes how the finite element method and the finite volume method can be successfully combined to derive two new families of thin plate and shell triangles with translational degrees of freedom as the only nodal variables. The simplest elements of the two families based on combining a linear interpolation of displacements with cell centred and cell vertex finite volume schemes are presented in detail. Examples of the good performance of the new rotation-free plate and shell triangles are given. Copyright © 2000 John Wiley & Sons, Ltd.

KEY WORDS: rotation-free; thin plate and shell triangles; finite elements; finite volumes

INTRODUCTION

The need for efficient plate and shell elements is essential for solving large-scale industrial problems such as the analysis of shell structures in civil, mechanical, naval and airspace engineering, the study of vehicle dynamics and crash-worthiness situations and the design of sheet metal forming processes among others. Despite recent advances in the field [1–3], the derivation of simple triangles capable of accurately representing the deformation of a plate or a shell structure under complex loading conditions is still nowadays a challenging topic of intensive research.

The development of plate (and shell) finite elements was initially based on the so called thin plate theory following Kirchhoff's main assumption of preserving orthogonality of the normals to the mid-plane [1, 4]. Indeed, most plates and shells can be classed as 'thin' structures and therefore Kirchhoff's theory can reproduce the essential features of the deformation in many practical cases. The well known problems to derive conforming C_1 continuous thin plate and shell elements motivated a number of authors to explore the possibilities of Reissner–Mindlin theory. This theory relaxes the normal orthogonality condition, thereby introducing the effect of shear deformation which can be of practical importance in thick situations, such as the analysis of some bridge slabs and, more important, it requires only C_0 continuity for the deflection and rotation fields. Unfortunately Reissner–Mindlin plate and shell elements suffer from the so called 'shear locking' deffect which pollutes the numerical solution in the thin limit. This defficiency has jeopardized the full success of Reissner–Mindlin plate/shell elements for practical engineering analysis, an exception

---

* Correspondence to: Eugenio Oñate, International Centre for Numerical methods in Engineering, Universidad Politécnica de Cataluña, edificio C1, Campus Norte UPC, Gran Capitán s/n, 08034 Barcelona, Spain. E-mail: onate@cimne.upc.es

perhaps being the four node quadrilateral based on an assumed shear strain formulation developed by Dvorkin and Bathe [5]. Thus, despite considerable efforts [6–23] there are not yet well established simple triangles which are currently used for solving large-scale industrial plate and shell problems.

This paper presents a general approach to derive very simple plate and shell triangular elements incorporating the displacements as the only nodal variables. The elements are based on Kirchhoff's thin plate theory and as such can be viewed as a return to the origins of plate and shell finite elements. Indeed for the applications in mind such as the analysis of standard thin plate and shell analysis, vehicle crash-worthiness and sheet stamping processes, Kirchhoff's theory suffices for practical purposes.

The idea of using the deflection as the only nodal variable for plate bending analysis is not new and many finite difference (FD) procedures are based on this approach [24]. The obvious difficulties of FD techniques are the treatment of boundary conditions and the problems for dealing with non-orthogonal or unstructured grids.

Several authors have tried to derive plate and shell finite elements with displacements as the nodal variables. So far the methods limit their applicability to triangular shapes only. The first attempt was probably due to Nay and Utku [25] who derived a rotation free thin plate triangle using a least-square quadratic approximation to describe the deflection field within the patch surrounding a node in terms of the deflections of the patch nodes. The stiffness matrix of the resulting three node plate triangle were computed by the standard minimum potential energy approach. A few years later Barnes [26] proposed a method for deriving a three node plate triangle with the nodal deflections as the only degrees of freedom (d.o.f.) based on the computation of the curvatures in terms of the normal rotations at the mid-side points determined from the nodal deflections of adjacent elements. This method was exploited by Hampshire *et al.* [27] assuming that the elements are hinged together at their common boundaries, the bending stiffness being represented by torsional springs resisting the rotations about the hinge lines. Phaal and Calladine [28, 29] proposed a similar class of rotation-free triangles for plate and shell analysis. Yang *et al.* [30] derived a family of triangular elements of this type for sheet stamping analysis based on so called bending energy augmented membrane approach which basically reproduces the hinge bending stiffness procedure of Hampshire *et al.* [27]. Brunet and Sabourin [31] proposed a different approach to compute the constant curvature field within each triangle in terms of the six node displacements of a macro-element. The triangle was successfully applied to non-linear shell analysis using an explicit dynamic approach. Rio *et al.* [32] have used the concept of side hinge bending stiffness to derive a thin shell triangle of 'translational' kind for explicit dynamic analysis of sheet stamping problems.

In 1993 Oñate and Cervera [33] proposed a general procedure based on finite volume concepts [34–36] for deriving thin plate elements of triangular and quadrilateral shapes with the nodal deflection as the only degree of freedom and presented a competitive and simple three d.o.f. triangle. In this work the ideas presented in [33] are extended to derive new rotation-free plate and shell elements. The basic ingredients of the derivation are a mixed Hu–Washizu formulation, a standard discretization of the plate surface into three node triangles, a linear finite element (FE) approximation of the displacement field within each triangle and a finite volume (FV) type approach for computing the curvature and bending moment fields within appropriate non-overlapping control domains. Basically two modalities of control domains will be considered here, leading each to a different plate triangle: the so called 'cell centred' patch formed by each individual triangle, leading to the BPT plate triangle and the BST shell triangle, and the 'cell vertex' domain formed
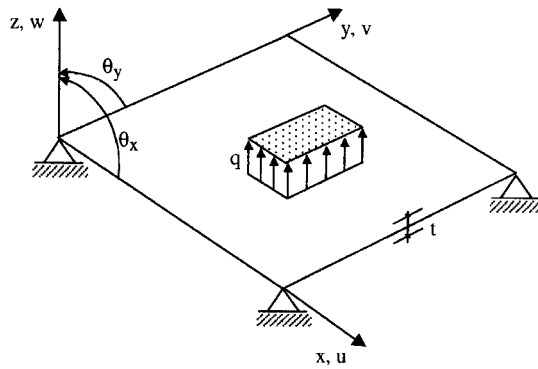
Figure 1. Sign convention for the deflection and the rotations in a plate

by the non-overlapping nodal regions, leading to the BPN and BSN plate and shell triangles, respectively.

The layout of the paper is the following. In the next section the basic concepts of Kirchhoff's plate theory are given and the set of governing equations emerging from the standard Hu–Washizu formulation are described. Next, details of the combined finite element/finite volume approach used in the formulation of the rotation free BPT and BPN plate triangles are described. An extension of the BPT element based on a linear least-square interpolation of the deflection gradients over an element patch is also presented. The relevant matrices and vectors for each case are given in explicit form. The formulation of the rotation-free BST and BSN shell triangles is then described as an extension of the parent thin plate formulation. Examples of the efficiency of the new triangles for a wide range of plate and shell problems are finally presented.

BASIC THEORY

Let us consider the plate of Figure 1. We will assume Kirchhoff's thin plate conditions to hold, i.e.

$$\theta_x = \partial w/\partial x \quad \text{and} \quad \theta_y = \partial w/\partial y \tag{1}$$

The curvatures field and the moment–curvature relationship can be expressed in the usual manner as

$$\boldsymbol{\kappa} = \mathbf{L}w, \quad \mathbf{m} = \mathbf{D}\boldsymbol{\kappa} \tag{2}$$

with

$$\boldsymbol{\kappa} = [\kappa_x, \kappa_y, \kappa_{xy}]^{\mathrm{T}}, \quad \mathbf{m} = [m_x, m_y, m_{xy}]^{\mathrm{T}}$$

$$\mathbf{L} = \left[-\frac{\partial^2}{\partial x^2}, -\frac{\partial^2}{\partial y^2}, -2\frac{\partial^2}{\partial x \partial y} \right]^{\mathrm{T}}, \quad \mathbf{D} = \frac{Et^3}{12(1-v^2)} \begin{bmatrix} 1 & v & 0 \\ v & 1 & 0 \\ 0 & 0 & \dfrac{1-v}{2} \end{bmatrix} \tag{3}$$

where E and v are the Young's modulus and the Poisson's ratio, respectively, and t is the plate thickness.

The set of governing equations will be expressed in integral form starting from the standard Hu–Washizu functional [1]

$$\Pi = \frac{1}{2} \iint_A \boldsymbol{\kappa}^{\mathrm{T}} \mathbf{D} \boldsymbol{\kappa} \, \mathrm{d}A - \iint_A [\mathbf{L}w - \boldsymbol{\kappa}]^{\mathrm{T}} \mathbf{m} \, \mathrm{d}A - \iint_A qw \, \mathrm{d}A \tag{4}$$

where q is the distributed loading and A is the area of the plate. Variation of Π with respect to $\boldsymbol{\kappa}$, $\mathbf{m}$ and w leads to the following three equations:

Constitutive equation

$$\iint_A \delta\boldsymbol{\kappa}^{\mathrm{T}}[\mathbf{D}\boldsymbol{\kappa} - \mathbf{m}] \, \mathrm{d}A = 0 \tag{5a}$$

Curvature-deflection equation

$$\iint_A \delta\mathbf{m}^{\mathrm{T}}[\mathbf{L}w - \boldsymbol{\kappa}] \, \mathrm{d}A = 0 \tag{5b}$$

Equilibrium equation

$$\iint_A [\mathbf{L}\delta w]^{\mathrm{T}} \mathbf{m} \, \mathrm{d}A - \iint_A \delta w q \, \mathrm{d}A = 0 \tag{5c}$$

Equations (5a)–(5c) represent the global satisfaction over the plate of the constitutive, kinematic and equilibrium equations, respectively. Equations (5) are the basis of the FE/FV discretization to be presented next.

FINITE ELEMENT/FINITE VOLUME DISCRETIZATION

Let us consider an arbitrary discretization of the plate into standard three node triangles. The curvature and the bending moments are described by constant fields within appropriate *non-overlapping control domains* (also termed 'control volumes' in the FV literature [34–36]) covering the whole plate as

$$\mathbf{m} = \mathbf{I}_3 \mathbf{m}_p, \quad \delta\mathbf{m} = \mathbf{I}_3 \delta\mathbf{m}_p \tag{6a}$$

$$\boldsymbol{\kappa} = \mathbf{I}_3 \boldsymbol{\kappa}_p, \quad \delta\boldsymbol{\kappa} = \mathbf{I}_3 \delta\boldsymbol{\kappa}_p \tag{6b}$$

where $\mathbf{I}_3$ is the 3×3 unit matrix and $(\cdot)_p$ denotes constant values for the pth control domain.

Two modalities of control domains are considered: (a) that formed by a single triangular element (Figure 2(a)) and (b) the control domain formed by one-third of the areas of the elements surrounding a node (Figure 2(b)). The two options are termed in the FV literature 'cell centred' and 'cell vertex' schemes, respectively.

Note that in the cell centred scheme each control domain coincides with a standard three node finite element triangle. Alternatively in the cell vertex scheme a control domain is contributed by different elements, as shown in Figure 2(b).

It is also useful to define the term 'patch of elements' associated to a control domain. In the cell centred scheme (Figure 2(a)) this patch is always formed by four elements (except in elements sharing a boundary segment), whereas in the cell vertex scheme the number of elements in the patch is variable (Figure 2(b)).

Remark 1. The name 'Cell Centred' (CC) indicates that the chosen variables (i.e. the curvatures and bending moments) are 'sampled' at the center of the cells discretizing the analysis domain (i.e. the three node triangles). Similarly a 'Cell Vertex' (CV) scheme denotes that the variables are sampled at the corners (i.e. the nodes) of the discretizing grid. This terminology has suffered some controversial interpretations in the past (for instance in [33, 34] a different criterion was chosen). The meaning given here to the CC and CV schemes corresponds to above definition.

The constant curvature and bending moment fields within each control domain are expressed next in terms of the nodal deflections associated to the corresponding element patch.

The area integrals in equations (5) can be written as sum of contributions over the different control domains taking into account equations (6) as

Constitutive equation

$$\sum_p \iint_{A_p} \delta\boldsymbol{\kappa}_p^{\mathrm{T}}[\mathbf{D}\boldsymbol{\kappa}_p - \mathbf{m}_p]\,\mathrm{d}A = 0 \tag{7}$$

where A_p is the area of the pth control domain.

Recalling that the virtual curvatures are arbitrary, gives

$$\boxed{\mathbf{m}_p = \mathbf{D}_p\boldsymbol{\kappa}_p} \tag{8a}$$

$$\mathbf{D}_p = \frac{1}{A_p}\iint_{A_p}\mathbf{D}\,\mathrm{d}A \tag{8b}$$

where $\mathbf{D}_p$ is the average constitutive matrix over a control domain. Equation (8a) defines the constant bending moment field over the control domain in terms of the corresponding constant curvatures.

Curvature-deflection equation

$$\sum_p \iint_{A_p} \delta\mathbf{m}_p^{\mathrm{T}}[\mathbf{L}w - \boldsymbol{\kappa}_p]\,\mathrm{d}A = 0 \tag{9}$$

Taking into account that the virtual bending moments are arbitrary, gives

$$\boldsymbol{\kappa}_p = \frac{1}{A_p}\iint_{A_p}\mathbf{L}w\,\mathrm{d}A \tag{10}$$

A simple integration by parts of the r.h.s. of equation (10) leads to

$$\boxed{\boldsymbol{\kappa}_p = \frac{1}{A_p}\int_{\Gamma_p}\mathbf{T}\boldsymbol{\nabla}w\,\mathrm{d}\Gamma} \tag{11}$$

where

$$\mathbf{T} = \begin{bmatrix} -n_x & 0 & -n_y \\ 0 & -n_y & -n_x \end{bmatrix}^{\mathrm{T}}, \quad \boldsymbol{\nabla} = \left\{ \begin{array}{c} \dfrac{\partial}{\partial x} \\[2mm] \dfrac{\partial}{\partial y} \end{array} \right\} \tag{12}$$
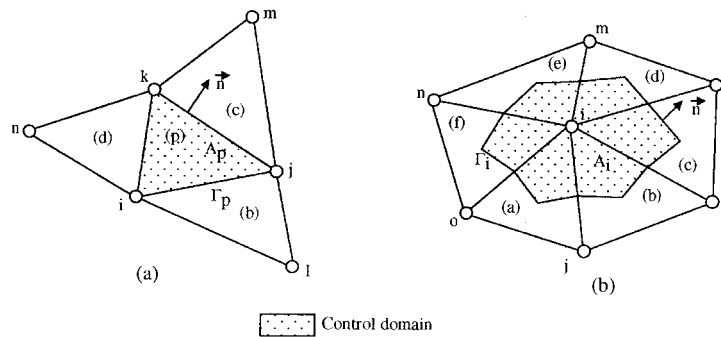
Figure 2. (a) Cell centred and (b) cell vertex finite volume schemes. BPT and BPN triangles

and $\mathbf{n} = [n_x, n_y]^T$ is the outward unit normal to the boundary Γ_p surrounding the control domain (Figure 2).

Equation (11) defines the curvatures for each control volume in terms of the deflection gradients along its boundaries. The transformation of the area integral of equation (10) into the line integral of equation (11) is typical of finite volume methods [33–36].

Remark 2. The computation of the line integral in equation (11) poses a difficulty for cases where the deflection gradient is discontinuous at the control volume boundaries and some smoothing procedure is then required. This issue is discussed in more detail in a later section.

Equilibrium equation
Equation (5c) can be expressed as

$$\sum_p \iint_{A_p} [\mathbf{L}\delta w]^T \mathbf{m}_p \, \mathrm{d}A - \iint_A \delta w q \, \mathrm{d}A = 0 \tag{13}$$

Integrating by parts the first integral in equation (13) and recalling that the bending moments are constant within each control domain, gives

$$\sum_p \left(\int_{\Gamma_p} [\mathbf{T}\boldsymbol{\nabla}\delta w]^T \, \mathrm{d}\Gamma \right) \mathbf{m}_p - \iint_A \delta w q \, \mathrm{d}A = 0 \tag{14}$$

Substituting equations (8a) and (11) into equation (14) finally gives

$$\sum_p \left(\int_{\Gamma_p} [\mathbf{T}\boldsymbol{\nabla}\delta w]^T \, \mathrm{d}\Gamma \right) \frac{1}{A_p} \mathbf{D}_p \int_{\Gamma_p} \mathbf{T}\boldsymbol{\nabla}w \, \mathrm{d}\Gamma - \iint_A \delta w q \, \mathrm{d}A = 0 \tag{15}$$

Equation (15) is the basis for deriving the final set of algebraic equations, after appropriate discretization of the deflection field as described next.

Derivation of the discretized equations

The final step is to discretize the deflection field. The simplest option is to interpolate linearly the deflection within each triangular element in terms of the nodal values in the standard finite element manner [1] as

$$w = \sum_{i=1}^{3} N_i w_i = \mathbf{N}^{(e)} \mathbf{w}^{(e)} \tag{16}$$

with $\mathbf{N}^{(e)} = [N_1, N_2, N_3]$ and $\mathbf{w}^{(e)} = [w_1, w_2, w_3]^{\mathrm{T}}$. In equation (16) w_i denotes the nodal deflection values and N_i are the standard linear shape functions of the three node triangle [1]. Substituting equations (16) into (11) gives

$$\boldsymbol{\kappa}_p = \frac{1}{A_p} \int_{\Gamma_p} \mathbf{T} \boldsymbol{\nabla} \mathbf{N}^{(e)} \mathbf{w}^{(e)} = \mathbf{B}_p \mathbf{w}_p \tag{17}$$

where vector $\mathbf{w}_p$ lists the deflections of the nodes linked to the *p*th control domain and $\mathbf{B}_p$ is the curvature matrix relating the constant curvature field within a control domain and the nodal deflections associated to the control domain. The computation of matrix $\mathbf{B}_p$ is different for cell vertex and cell centred schemes and the details are given in next sections.

Substituting equations (16) into (15) gives the final system of algebraic equations as

$$\mathbf{K}\mathbf{w} = \mathbf{f} \tag{18}$$

where vector $\mathbf{w}$ contains the nodal deflections of all mesh nodes. The global stiffness matrix $\mathbf{K}$ can be obtained by assembling the stiffness contributions from the different control domains given by

$$\mathbf{K}_p = [\mathbf{B}_p]^{\mathrm{T}} \mathbf{D}_p \mathbf{B}_p A_p \tag{19}$$

The components of the nodal force vector $\mathbf{f}$ in equation (18) are obtained as in standard C_0 linear finite element triangles [1], i.e.

Point loading

$$f_i = p_i \tag{20}$$

where p_i is the point load acting on the *i*th node

Distributed loading

$$f_i^{(e)} = \iint_{A^{(e)}} N_i q(x) \, \mathrm{d}A \tag{21}$$

The global nodal force component f_i is obtained by assembling the element contributions $f_i^{(e)}$ in the standard finite element manner. For a constant distributed load q this gives

$$f_i = \sum_e \frac{q A^{(e)}}{3} \tag{22}$$

where the sum extends to all triangular elements sharing the *i*th node and $A^{(e)}$ is the area of element *e*.

Box I. Matrix $\mathbf{B}_p$ for the 3 d.o.f. basic plate triangle (BPT)

$$\mathbf{B}_p = \frac{1}{A_p} \begin{bmatrix} \begin{array}{c} y_{ij}\bar{b}_i^{(b)} + y_{ki}\bar{b}_i^{(d)} \\ -x_{ij}\bar{c}_i^{(b)} - x_{ki}\bar{c}_i^{(d)} \\ \left[y_{ij}\bar{c}_i^{(b)} - x_{ij}\bar{b}_i^{(b)} \right. \\ \left. + y_{ki}\bar{c}_i^{(d)} - x_{ki}\bar{b}_i^{(d)} \right] \end{array} & \begin{array}{c} y_{ij}\bar{b}_j^{(b)} + y_{jk}\bar{b}_j^{(c)} \\ -x_{ij}\bar{c}_j^{(b)} - x_{jk}\bar{c}_j^{(c)} \\ \left[y_{ij}\bar{c}_j^{(b)} - x_{jk}\bar{b}_j^{(b)} \right. \\ \left. + y_{jk}\bar{c}_j^{(c)} - x_{jk}\bar{b}_j^{(c)} \right] \end{array} & \begin{array}{c} y_{jk}\bar{b}_k^{(c)} + y_{ki}\bar{b}_k^{(d)} \\ -x_{jk}\bar{c}_k^{(c)} - x_{ki}\bar{c}_k^{(d)} \\ \left[y_{jk}\bar{c}_k^{(c)} - x_{jk}\bar{b}_k^{(c)} \right. \\ \left. + y_{ki}\bar{c}_k^{(d)} - x_{ki}\bar{b}_k^{(d)} \right] \end{array} \\[3em] \begin{array}{c} y_{ij}\bar{b}_l^{(b)} \\ -x_{ij}\bar{c}_l^{(b)} \\ y_{ij}\bar{c}_l^{(b)} - x_{ij}\bar{b}_l^{(b)} \end{array} & \begin{array}{c} y_{jk}\bar{b}_m^{(c)} \\ -x_{jk}\bar{c}_m^{(c)} \\ y_{jk}\bar{c}_m^{(c)} - x_{jk}\bar{b}_m^{(c)} \end{array} & \begin{array}{c} y_{ki}\bar{b}_n^{(d)} \\ -x_{ki}\bar{c}_n^{(d)} \\ y_{ki}\bar{c}_n^{(d)} - x_{ki}\bar{c}_n^{(d)} \end{array} \end{bmatrix}$$

$$\bar{b}_i^{(e)} = \frac{b_i^{(e)}}{2A_p^{(e)}}, \quad \bar{c}_i^{(e)} = \frac{c_i^{(e)}}{2A_p^{(e)}}, \quad b_i^{(e)} = y_j^{(e)} - y_k^{(e)} \quad c_i = x_k^{(e)} - x_j^{(e)}, \text{ etc.}, \quad A_p = A^{(p)}$$

CELL CENTERED PATCH BPT ELEMENT

The evaluation of the constant curvature field in equation (11) requires the computation of the deflection gradient along the control domain boundaries. This poses a difficulty in cell centred configurations where each control domain coincides with an individual element. Here if the deflection is linearly interpolated within each triangle, then the term ∇w is discontinuous at the element sides. A simple method to overcome this problem proposed by Oñate and Cervera [33] is to compute the deflection gradients at the triangle sides as the average value of the gradients contributed by the two elements sharing the side. The constant curvature field for each control domain can be expressed in this case as

$$\boldsymbol{\kappa}_p = \frac{1}{A_p} \sum_{j=1}^{3} \frac{l_j^{(p)}}{2} \mathbf{T}_j^{(p)} \left[\nabla \mathbf{N}^{(p)} \mathbf{w}^{(p)} + \nabla \mathbf{N}^{(k)} \mathbf{w}^{(k)} \right] = \mathbf{B}_p \mathbf{w}_p \tag{23a}$$

with

$$\mathbf{w}_p = [w_i, w_j, w_k, w_l, w_m, w_n]^{\mathrm{T}} \tag{23b}$$

In equation (23a) the sum extends over the three sides of element p coinciding with the pth control domain, $\mathbf{T}_j^{(p)}$ is the transformation matrix of equation (12) for side j, $l_j^{(p)}$ are the lengths of the element sides, $A_p = A^{(p)}$ is the area of the fth triangle and superindex k refers to each of the elements adjacent to element p ($k = a, b, c$ for $j = 1, 2, 3$. See Figure 2(a)).

The computation of the curvature matrix is simple noting that the gradients of the shape functions are constant within each element. The explicit form of matrix $\mathbf{B}_p$ is given in Box I.

Note that $\mathbf{B}_p$ in this case is a 3×6 matrix relating the deflections of the six nodes of the four element patch contributing to the control domain. Consequently the stiffness matrix $\mathbf{K}_p$ is a 6×6 matrix.

The resulting plate element is identical to that derived by Oñate and Cervera [33] and it is termed BPT (for Basic Plate Triangle). The element can be viewed as a standard finite element
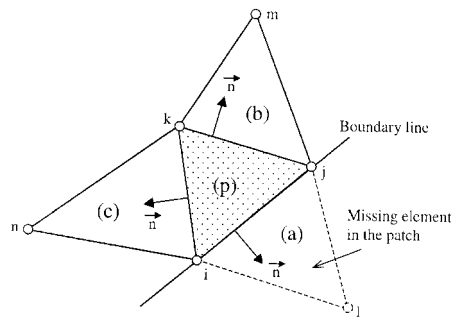
Figure 3. Basic plate triangle (BPT) next to a boundary line

plate triangle with one degree of freedom per node and a wider bandwidth, as each element is linked to its neighbours through equation (23a).

Boundary conditions for the BPT element

The implementation of the boundary conditions is straightforward and the main difference with standard finite elements is that the conditions on the prescribed rotations must be imposed when the curvature matrices $\mathbf{B}_p$ are being built. The different situations are considered next.

A BPT element with a side along a boundary edge has one of the elements contributing to the patch missing. This is simply taken into account by ignoring this contribution when performing the average of the deflection gradient in equation (23a). Thus, if side 1 corresponding to nodes ij lies on the boundary (Figure 3), the curvature field for the control domain is obtained by

$$\boldsymbol{\kappa}_p = \frac{l_{ij}}{A_p}\mathbf{T}_1^{(p)}\boldsymbol{\nabla}\mathbf{N}^{(p)}\mathbf{w}^{(p)} + \frac{1}{A_p}\sum_{j=2}^{3}\frac{l_j^{(p)}}{2}\mathbf{T}_j^{(p)}[\boldsymbol{\nabla}\mathbf{N}^{(p)}\mathbf{w}^{(p)} + \boldsymbol{\nabla}\mathbf{N}^{(k)}\mathbf{w}^{(k)}] = \mathbf{B}_p\mathbf{w}_p \qquad (24)$$

Additional conditions must be imposed in the case of boundary edges where the rotations and/or the deflections are constrained as explained next.

Clamped edge ($w = \boldsymbol{\nabla}w = 0$)

The conditions on the rotations are simply imposed by disregarding the contributions from the clamped edges when computing the sum along the element sides in equation (23a). For instance, if side ij is clamped this simply implies making zero the first term in the r.h.s. of equation (24).

The condition $w = 0$ on the nodes laying on clamped edges is prescribed at the equation solution level in the standard manner.

Symmetry edge ($\partial w/\partial x = 0$ or $\partial w/\partial y = 0$)

The condition of zero rotation is imposed by neglecting the contribution from the prescribed rotation term ($\partial w/\partial x$ or $\partial w/\partial y$) at the symmetry edge when computing equation (23a).

Simply supported edge ($w = \partial w/\partial s = 0$)

The condition $\partial w/\partial s = 0$, where s is the boundary direction, is simply imposed by prescribing $w = 0$ in the boundary nodes at the global equation solution level in the standard fashion. The effect of the 'missing' contributing element at the boundary edge is accounted for by skipping the averaging of the deflection gradient for that edge as described above.

BPT1 ELEMENT

An interesting alternative to the BPT element can be derived by defining a linear deflection gradient field over the four element patch. The simplest procedure is to use a least-square approximation of the deflection gradients computed at the centroids of the four elements contributing to the control domain (Figure 2(a)). This avoids the averaging procedure of equation (23a) as the deflection gradient is now continuous over the control volume. The basic ingredients of the element, termed BPT1, are given next.

The deflection gradient is defined linearly over the four elements patch as

$$\boldsymbol{\nabla} w = \left\{ \begin{array}{c} a_1 \\ a_2 \end{array} \right\} + \left\{ \begin{array}{c} b_1 \\ b_2 \end{array} \right\} x + \left\{ \begin{array}{c} c_1 \\ c_2 \end{array} \right\} y = \mathbf{a} + \mathbf{b}x + \mathbf{c}y \tag{25}$$

The $\mathbf{a}, \mathbf{b}$ and $\mathbf{c}$ parameters are obtained by minimizing the following quadratic form:

$$\mathbf{J}_p = \sum_{i=1}^{4} [(\boldsymbol{\nabla} w)_i - (\mathbf{a} + \mathbf{b}x_i + \mathbf{c}y_i)]^2 \tag{26}$$

with respect to the parameters a_i, b_i, c_i.

In equation (26) $(\boldsymbol{\nabla} w)_i$ are the deflection gradients computed at the centroid (x_i, y_i) of each of the four elements linked to the pth control domain. It can be easily shown that

$$(\boldsymbol{\nabla} w)_i = \frac{1}{2A^{(i)}} \sum_{j=1}^{3} \left\{ \begin{array}{c} \alpha_j^{(i)} \\ \beta_j^{(i)} \end{array} \right\} w_j \tag{27}$$

with $\alpha_j^{(i)} = y_k^{(i)} - y_l^{(i)}$, $\beta_j^{(i)} = x_l^{(i)} - x_k^{(i)}$ for an element with nodes j, k, l [1].

In equation (27) $A^{(i)}$ is the area of the ith element and $x_j^{(i)}$, $y_j^{(i)}$, $j = 1, 2, 3$, are the coordinates of the element nodes.

Minimization of $\mathbf{J}_p$ gives

$$[a_1, b_1, c_1]^{\mathrm{T}} = \mathbf{C}^{-1}\mathbf{GS}_x\mathbf{w}_p \tag{28a}$$

$$[a_2, b_2, c_2]^{\mathrm{T}} = \mathbf{C}^{-1}\mathbf{GS}_y\mathbf{w}_p \tag{28b}$$

where $\mathbf{w}_p$ is given by equation (23b) and the form of the matrices $\mathbf{C}, \mathbf{G}, \mathbf{S}_x$ and $\mathbf{S}_y$ is shown in Box II.
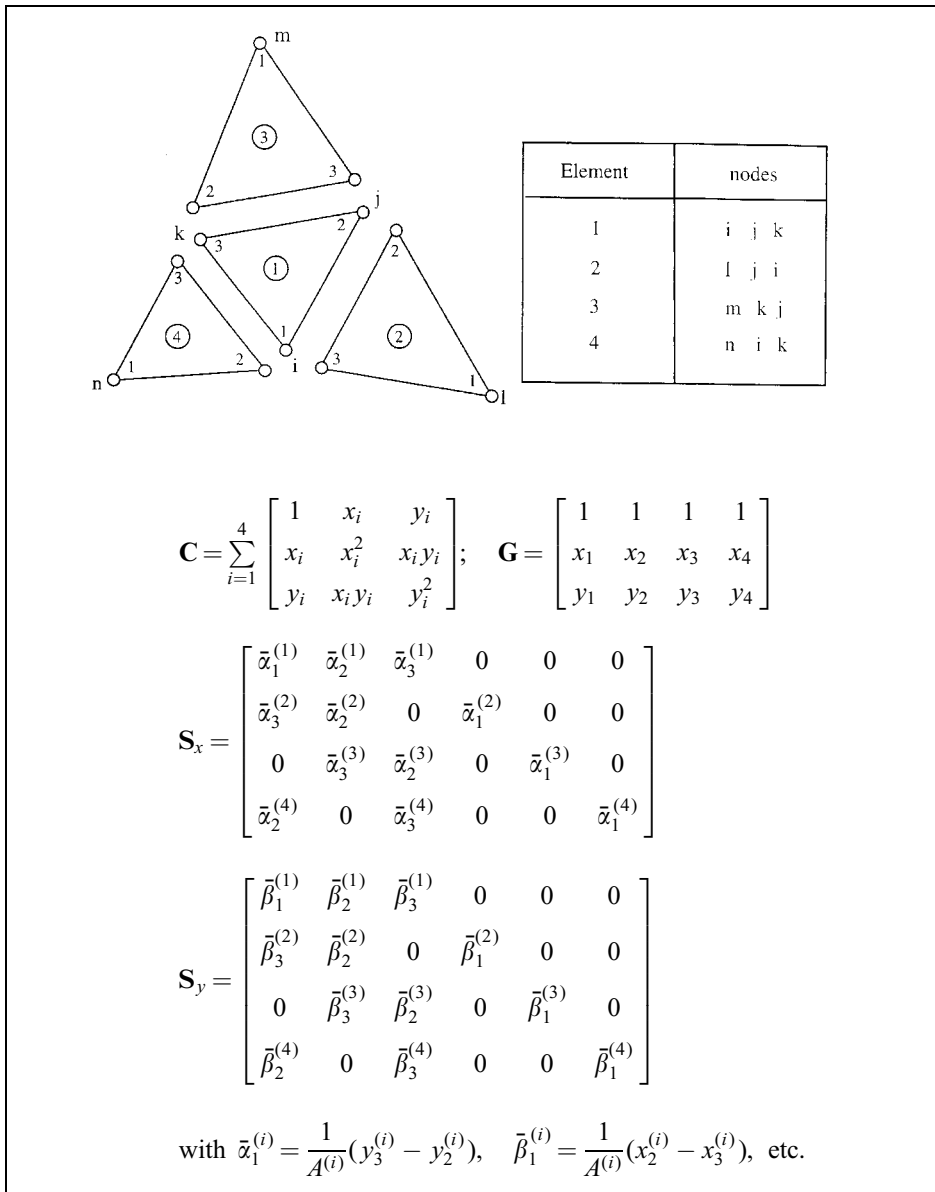
Equation (25) can be used to compute the curvature vector for each control domain using equation (11) as

$$\boldsymbol{\kappa}_p = \frac{1}{A_p} \int_{\Gamma_p} \mathbf{T}[\mathbf{a} + \mathbf{b}x + \mathbf{c}y]\mathrm{d}\Gamma = \frac{1}{A_p} \sum_{j=1}^{3} \mathbf{T}_j^{(p)}[\mathbf{a} + \mathbf{b}x_j + \mathbf{c}y_j]l_j = \mathbf{B}_p\mathbf{w}_p \tag{29}$$

where the sum extends to the three edges of the control domain, x_j, y_j are the coordinates of the mid-point of the jth edge and l_j is the edge length. The expression of $\mathbf{B}_p$ in this case can be easily deduced substituting equations (28) into equation (29).

The treatment of the boundary conditions follows the same procedure as for the BST element. Naturally in a control volume sharing a boundary edge, the linear interpolation of the deflection field is then exact as only three elements are involved in the approximation. Also, the contribution of edges where the rotation is prescribed to a zero value is neglected in the sum of equation (29).

Box II. Matrices involved in the derivation of the BPT1 element

$$\mathbf{C} = \sum_{i=1}^{4} \begin{bmatrix} 1 & x_i & y_i \\ x_i & x_i^2 & x_i y_i \\ y_i & x_i y_i & y_i^2 \end{bmatrix}; \quad \mathbf{G} = \begin{bmatrix} 1 & 1 & 1 & 1 \\ x_1 & x_2 & x_3 & x_4 \\ y_1 & y_2 & y_3 & y_4 \end{bmatrix}$$

$$\mathbf{S}_x = \begin{bmatrix} \bar{\alpha}_1^{(1)} & \bar{\alpha}_2^{(1)} & \bar{\alpha}_3^{(1)} & 0 & 0 & 0 \\ \bar{\alpha}_3^{(2)} & \bar{\alpha}_2^{(2)} & 0 & \bar{\alpha}_1^{(2)} & 0 & 0 \\ 0 & \bar{\alpha}_3^{(3)} & \bar{\alpha}_2^{(3)} & 0 & \bar{\alpha}_1^{(3)} & 0 \\ \bar{\alpha}_2^{(4)} & 0 & \bar{\alpha}_3^{(4)} & 0 & 0 & \bar{\alpha}_1^{(4)} \end{bmatrix}$$

$$\mathbf{S}_y = \begin{bmatrix} \bar{\beta}_1^{(1)} & \bar{\beta}_2^{(1)} & \bar{\beta}_3^{(1)} & 0 & 0 & 0 \\ \bar{\beta}_3^{(2)} & \bar{\beta}_2^{(2)} & 0 & \bar{\beta}_1^{(2)} & 0 & 0 \\ 0 & \bar{\beta}_3^{(3)} & \bar{\beta}_2^{(3)} & 0 & \bar{\beta}_1^{(3)} & 0 \\ \bar{\beta}_2^{(4)} & 0 & \bar{\beta}_3^{(4)} & 0 & 0 & \bar{\beta}_1^{(4)} \end{bmatrix}$$

with $\bar{\alpha}_1^{(i)} = \dfrac{1}{A^{(i)}}(y_3^{(i)} - y_2^{(i)})$, $\quad \bar{\beta}_1^{(i)} = \dfrac{1}{A^{(i)}}(x_2^{(i)} - x_3^{(i)})$, etc.

Remark 3. The curvature matrix for the BPT1 element can be readily derived by using the original form of equation (10) as the second derivatives of the deflection field can be directly computed from equation (25). The result is obviously the same in both cases.

Remark 4. The interpolation of the deflection field can be enhanced using weighted least-square interpolation techniques [37].
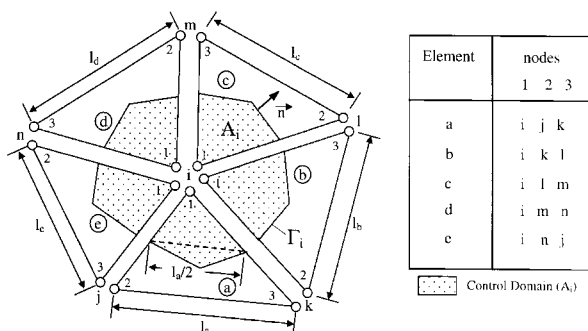
Figure 4. BPN element. Example of a typical control domain and numbering of nodes

Remark 5. The performance of the BPT and BPT1 elements is identical for regular structured meshes as the stiffness matrices are the same in both cases. In non-structured meshes the performance of the BPT1 element is slightly superior as it will be shown in the examples.

CELL VERTEX PATCH. BPN ELEMENT

As mentioned earlier, a different class of rotation-free plate triangles can be derived starting from the so called cell vertex finite volume scheme (Figure 2(b)). The advantage of the cell vertex scheme is that the deflection gradient is now continuous along the control domain boundaries. This allows to compute directly the constant curvature vector over the control domain as

$$\boldsymbol{\kappa}_i = \frac{1}{A_i} \int_{\Gamma_i} \mathbf{T} \boldsymbol{\nabla} \mathbf{N}_i \mathbf{w}_i \, \mathrm{d}\Gamma = \mathbf{B}_i \mathbf{w}_i \tag{30}$$

where $\mathbf{N}_i$ contains contributions from the shape functions from all the elements participating in the ith nodal control domain. Equation (30) can be rewritten in a simpler form taking into account that the deflection gradients are constant within each element, as

$$\boldsymbol{\kappa}_i = \frac{1}{A_i} \sum_j \frac{l_j}{2} \mathbf{T}_j \boldsymbol{\nabla} \mathbf{N}^{(j)} \mathbf{w}^{(j)} = \mathbf{B}_i \mathbf{w}_i \tag{31}$$

where the sum extends over the n_i elements contributing to the ith control domain (for instance $n_i = 5$ in the patch of Figure 4), l_j is the external side of element j, $\mathbf{T}_j$ is the transformation matrix of equation (12) linked to the side l_j, superindex j refers to element values and $A_i = \frac{1}{3} \sum_{k=1}^{n_i} A^{(k)}$ where $A^{(k)}$ is the area of element k.

The computation of the curvature matrix $\mathbf{B}_i$ is not so straightforward in this case as its size depends on the variable number of nodes over the element patch contributing to a nodal control domain (see Figure 4).

Typically

$$\underset{3 \times n}{\mathbf{B}_i} = [\overset{1}{\mathbf{B}^i} \quad \overset{2}{\mathbf{B}^a}, \ldots, \quad \overset{p_n}{\mathbf{B}^r}] \tag{32}$$

Box III. Example of derivation of the curvature matrix for the BPN control domain of Figure 4

$$\mathbf{B}_i = [\mathbf{B}^i, \mathbf{B}^j, \mathbf{B}^k, \mathbf{B}^l, \mathbf{B}^m, \mathbf{B}^n]$$

$$\mathbf{B}^i = \frac{1}{2A_i} \left[l_a \mathbf{T}_a \mathbf{G}_1^{(a)} + l_b \mathbf{T}_b \mathbf{G}_1^{(b)} + l_c \mathbf{T}_c \mathbf{G}_1^{(c)} + l_d \mathbf{T}_d \mathbf{G}_1^{(d)} + l_e \mathbf{T}_e \mathbf{G}_1^{(e)} \right]$$

$$\mathbf{B}^j = \frac{1}{2A_i} \left[l_a \mathbf{T}_a \mathbf{G}_2^{(a)} + l_e \mathbf{T}_e \mathbf{G}_3^{(e)} \right]$$

$$\mathbf{B}^k = \frac{1}{2A_i} \left[l_a \mathbf{T}_a \mathbf{G}_3^{(a)} + l_b \mathbf{T}_b \mathbf{G}_2^{(b)} \right]$$

$$\mathbf{B}^l = \frac{1}{2A_i} \left[l_b \mathbf{T}_b \mathbf{G}_3^{(b)} + l_c \mathbf{T}_c \mathbf{G}_2^{(c)} \right]$$

$$\mathbf{B}^m = \frac{1}{2A_i} \left[l_c \mathbf{T}_c \mathbf{G}_3^{(c)} + l_d \mathbf{T}_d \mathbf{G}_2^{(d)} \right]$$

$$\mathbf{B}^n = \frac{1}{2A_i} \left[l_d \mathbf{T}_d \mathbf{G}_3^{(d)} + l_e \mathbf{T}_e \mathbf{G}_2^{(e)} \right]$$

$$\mathbf{G}_i^{(k)} = \boldsymbol{\nabla} N_i^{(k)} = \frac{1}{2A^{(k)}} \left\{ \begin{array}{c} b_i \\ c_i \end{array} \right\}^{(k)}, \quad b_i^{(k)} = y_j^{(k)} - y_k^{(k)}, \quad c_i^{(k)} = x_k - x_j^{(k)}$$

where p_n is the number of nodes in the patch (i.e. $p_n = 6$ in the patch of Figure 4) and superindexes $i, a, \ldots, r$ refer to global node numbers. An explicit expression of the nodal curvature matrix $\mathbf{B}^i$ can be found as

$$\underset{3 \times 1}{\mathbf{B}^i} = \frac{1}{2A_i} \sum_k l_k \mathbf{T}_k \boldsymbol{\nabla} N_j^{(k)} \tag{33}$$

where the sum extends now over the elements sharing node i within the patch and j is the local number of node i within element k. An example of matrix $\mathbf{B}_i$ for a typical control domain is shown in Box III.

It is important to note that $\mathbf{B}_i$ is in this case the *global curvature matrix* for the central ith node. Thus, the product $\mathbf{B}_i^{\mathrm{T}} \mathbf{D}_i \mathbf{B}_i A_i$ provides the ith row of the global stiffness matrix. This simplifies the assembly and solution process as the global stiffness equations for a node can be elliminated once they are computed.

Indeed the standard 'element' stiffness matrix can be found by adding the contribution of the three internal domains participating into each triangular element as shown in Figure 5. This, however, has been found not useful for practical purposes and the direct assembly of the control domain contributions as explained above is recommended.
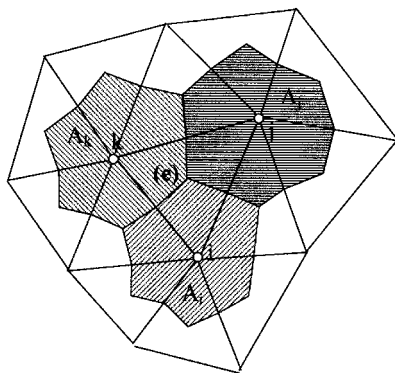
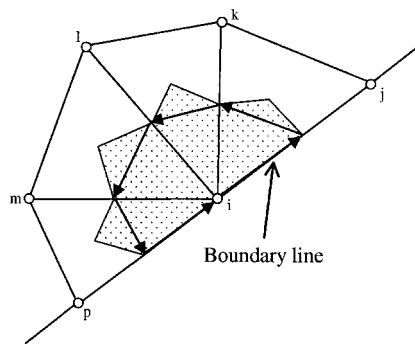Figure 5. Contribution of control domains to a BPN triangular element in the cell vertex scheme

Figure 6. BPN element. Control domain sharing a boundary line. Integration path for computation of curvature matrix

This plate element is termed BPN (for Basic Plate Nodal patch). Note that the concept of 'element' here is generalized as the BPN element combines a standard finite element interpolation with non-standard integration domains.

Boundary conditions for the BPN element

The method for imposing the boundary conditions in the BPN element follows the lines previously explained for the BPT element. The procedure is now simpler as the deflection gradient now is continuous along the control domain boundary which intersects the central node in this case (Figure 6). As usual, the conditions on nodal deflections are imposed at the global solution level while the prescribed rotations must be treated when building the curvature matrix.

Clamped and symmetry edges
Zero rotation conditions at clamped and symmetry edges are simply imposed by elliminating the contributions from these rotation terms in the sum of equation (31).

Simple supported edges
The condition $\partial w/\partial s = 0$ along an edge direction is simple accounted for by prescribing the deflections of the edge nodes to a zero value at the global solution level.

Free edges
No special treatment for the rotations is required at free edges. Advantage can be taken from the mixed formulation in this case by prescribing the edge bending moments M_n and M_{sn} to a zero value. This can be simply done by eliminating the contributions from these moments at free edge patches by making zero the appropriate rows in the constitutive matrix **D**. Indeed if the free edge is not parallel to one of the cartesian axes a transformation of the constitutive equation to edge axes is then necessary.

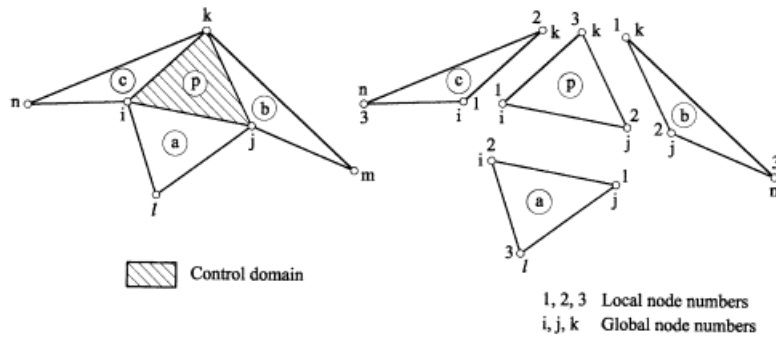This procedure can also be applied to impose the condition $M_n = 0$ at simply supported edges.

Figure 7. BST element. Control domain and four elements patch

BASIC SHELL TRIANGLE (BST)

The BPT element of previous section can be combined with the standard Constant Strain Triangle (CST) [1] to model membrane behaviour. The resulting rotation-free shell element is called Basic Shell Triangle (BST). The nodal degrees of freedom of the BST element are the three displacements. Thus, the computational cost of the BST element is equivalent to that of a standard membrane element, while it incorporates full bending effects. Details of the derivation of the BST element are given below.

BST element. Bending stiffness matrix

Figure 7 shows the patch of four shell triangles typical of the Cell Centered (CC) finite volume scheme. As usual in the CC scheme the control domain coincides with an individual element. Also in Figure 7 the local and global node numbering scheme chosen is shown. A clear definition of local and global node numbers is essential for the derivation of the BST element stiffness matrix as shown next.

Figure 8 shows the local element axes $x'y'z'$ where x' is parallel to side 1–2 (or i–j) and in the direction of increasing local node numbers, z' is a direction orthogonal to the element defining the unit normal vector $\mathbf{n}$ and y' is obtained by cross product of vectors along z' and x'. A side co-ordinate system is also defined (see Figures 8 and 9) including side unit vectors $\mathbf{s}, \mathbf{t}$ and $\mathbf{n}$. Vector $\mathbf{s}$ is aligned along the side following the directions of increasing global node numbers, $\mathbf{n}$ is the normal vector parallel to the z' local axis and $\mathbf{t} = \mathbf{n} \wedge \mathbf{s}$.

Let us now express the local rotations $\theta_{x'}, \theta_{y'}$ along each side in terms of the tangential and normal side rotations θ_s and θ_n. The sign for the rotations follows the criterion of Figures 8 and 9.

The transformation relating local and side rotations is written as

$$\boldsymbol{\theta}'^{(e)} = \left\{ \begin{array}{c} \theta_{x'} \\ \theta_{y'} \end{array} \right\}^{(e)} = \left[\begin{array}{cc} c_{ij} & -s_{ij} \\ s_{ij} & c_{ij} \end{array} \right]^{(e)} \left\{ \begin{array}{c} \theta_{s_{ij}} \\ \theta_{n_{ij}} \end{array} \right\}^{(e)} = \hat{\mathbf{T}}_{ij}\hat{\boldsymbol{\theta}}'_{ij} \tag{34}$$

where $\theta_{s_{ij}}$ and $\theta_{n_{ij}}$ are the tangential and normal rotations along side ij of element e, $\theta_{x'} = \partial w'/\partial x'$, $\theta_{y'} = \partial w'/\partial y'$ and $c_{ij}^{(e)}$, $s_{ij}^{(e)}$ are the components of side vector $\mathbf{s}_{ij}^{(e)}$, i.e. $\mathbf{s}_{ij}^{(e)} = [c_{ij}^{(e)}, s_{ij}^{(e)}]^{\mathrm{T}}$.
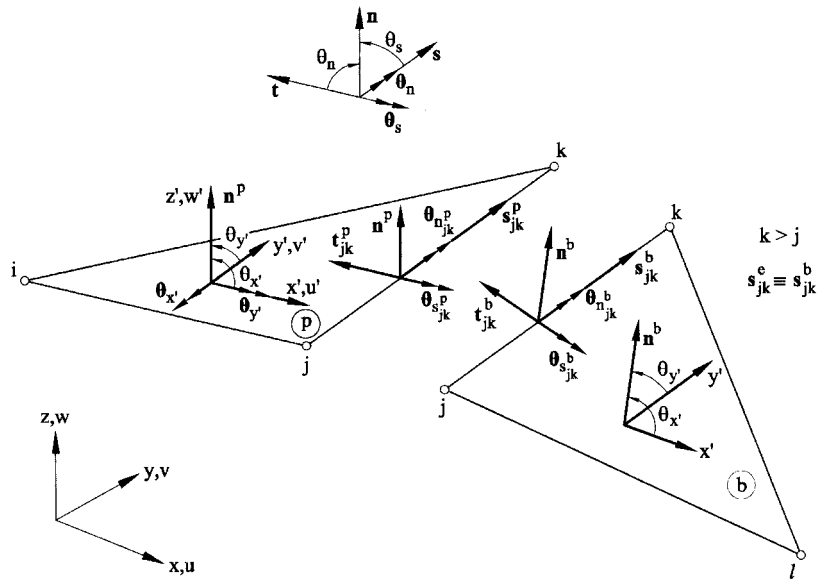
Figure 8. BST element. Definition of global, local and side co-ordinate systems
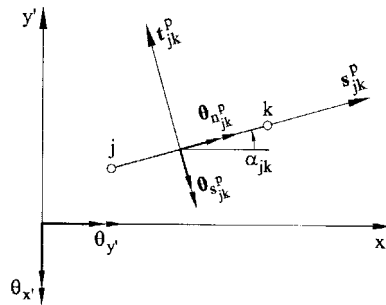

Figure 9. BST element. Transformation from side to local rotations

The definition of curvatures follows the lines given for the BPT element. The local curvatures over the control domain formed by the triangle ijk are given by (see equation (11))

$$\boldsymbol{\kappa}'_p = \frac{1}{A^{(p)}} \int_{\Gamma_p} \mathbf{T}\boldsymbol{\nabla}'w' \, \mathrm{d}\Gamma \tag{35}$$

where

$$\boldsymbol{\kappa}' = \left[-\frac{\partial^2 w'}{\partial x'^2}, \, -\frac{\partial^2 w'}{\partial y'^2}, \, -2\frac{\partial^2 w'}{\partial x'\partial y'} \right] \tag{36a}$$

$$\mathbf{T} = \begin{bmatrix} -t_{x'} & 0 & -t_{y'} \\ 0 & -t_{y'} & -t_{x'} \end{bmatrix}^{\mathrm{T}} \quad \text{and} \quad \boldsymbol{\nabla}' = \left\{ \begin{array}{c} \dfrac{\partial}{\partial x'} \\[2mm] \dfrac{\partial}{\partial y'} \end{array} \right\} \tag{36b}$$

where $t_{x'}, t_{y'}$ are the components of vector $\mathbf{t}$ in the x', y' co-ordinate system, respectively.

Recalling that $\boldsymbol{\theta}' = [\theta_{x'}, \theta_{y'}]^{\mathrm{T}} = \boldsymbol{\nabla}' w'$ and substituting equation (34) into (35), the curvature over the triangular control domain can be written as

$$\boldsymbol{\kappa}'_p = \frac{1}{A^{(p)}} [\mathbf{T}_{ij}^{(p)} \hat{\mathbf{T}}_{ij}^{(p)} \hat{\boldsymbol{\theta}}'_{ij} l_{ij} + \mathbf{T}_{jk}^{(p)} \hat{\mathbf{T}}_{jk}^{(p)} \hat{\boldsymbol{\theta}}'_{jk} l_{jk} + \mathbf{T}_{ki}^{(p)} \hat{\mathbf{T}}_{ki}^{(p)} \hat{\boldsymbol{\theta}}'_{ki} l_{ki}] \tag{37}$$

In the derivation of equation (37) it has been assumed that the local rotations are constant over each element side. This is a consequence of the linear interpolation chosen for the displacement field.

The tangential side rotations can be directly expressed in terms of the local deflections along the sides. For instance, for side jk

$$\theta_{s_{jk}}^{(p)} = \frac{w_k'^{(p)} - w_j'^{(p)}}{l_{jk}} \quad \text{for } k > j \tag{38}$$

where l_{jk} is the length of side jk.

Equation (38) introduces an approximation as the tangential rotation vectors of adjacent element sharing a side are not parallel. Therefore the tangential rotation are discontinuous along element sides, i.e. (see Figure 8)

$$\theta_{s_{jk}}^{(p)} = \frac{w_k'^{(p)} - w_j'^{(p)}}{l_{jk}} \neq \frac{w_k'^{(b)} - w_j'^{(b)}}{l_{jk}} = \theta_{s_{jk}}^{(b)} \tag{39}$$

The authors have found that this error has little relevance in practice. Note that the error diminishes for smooth shells as the mesh is refined. Thus, for quasi-coplanar sides $w_k'^{(p)} \simeq w_k'^{(b)}$, $w_j'^{(p)} \simeq w_j'^{(b)}$ and $\theta_{s_{jk}}^{(p)} \simeq \theta_{s_{jk}}^{(b)}$.

An alternative to ensure a continuous tangential side rotation is to define its value as the average of the tangential side rotations contributed by the two adjacent elements to the side, i.e.

$$\theta_{s_{jk}}^{(p)} = \tfrac{1}{2}(\theta_{s_{jk}}^{(p)} + \theta_{s_{jk}}^{(b)}) \tag{40}$$

The normal rotation vector has the same direction for the two elements sharing a side (Figure 8). A *continuous* value of the normal rotation along the side can be enforced by defining an average normal side rotation as

$$\theta_{n_{jk}}^{(p)} = \tfrac{1}{2}(\theta_{n_{jk}}^{(p)} + \theta_{n_{jk}}^{(b)}) \tag{41}$$

Using equation (34) the average normal rotation along the side can be expressed in terms of the normal deflections as

$$\theta_{n_{jk}}^{(p)} = \tfrac{1}{2}(\boldsymbol{\lambda}_{jk}^{(p)} \boldsymbol{\nabla}' w'^{(p)} + \boldsymbol{\lambda}_{jk}^{(b)} \boldsymbol{\nabla}' w'^{(b)}) \tag{42}$$

where

$$\boldsymbol{\lambda}_{jk}^{(p)} = [-s_{jk}^{(p)}, c_{jk}^{(p)}] \tag{43}$$

Box IV. BST element. Local curvature matrix for the control domain of Figure 7

$$\boxed{\boldsymbol{\kappa}'_p = \mathbf{S}_p \mathbf{w}'_p}$$

$$\mathbf{w}'_p = \left[w_i'^{(p)}, w_j'^{(p)}, w_k'^{(p)}, w_j'^{(a)}, w_i'^{(a)}, w_l'^{(a)}, w_k'^{(b)}, w_j'^{(b)}, w_m'^{(b)}, w_i'^{(c)}, w_k'^{(c)}, w_n'^{(c)} \right]^{\mathrm{T}}$$

$$\mathbf{S}_p = [\mathbf{S}_{ij}^{(p)}, \mathbf{S}_{jk}^{(p)}, \mathbf{S}_{ki}^{(p)}]; \quad \mathbf{S}_{ij}^{(p)} = \frac{l_{ij}}{A^{(p)}} \mathbf{T}_{ij}^{(p)} \hat{\mathbf{T}}_{ij}^{(p)} \mathbf{A}_{ij}^{(p)}$$

$$\mathbf{A}_{ij}^{(p)} = \begin{bmatrix} \alpha/l_{ij} & \beta/l_{ij} & 0 & 0 & 0 & 0 \\ \gamma_{iji}^{(p)} & \gamma_{ijj}^{(p)} & \gamma_{ijk}^{(p)} & \gamma_{ijj}^{(a)} & \gamma_{iji}^{(a)} & \gamma_{ijl}^{(a)} \end{bmatrix} \mathbf{0}_3 \quad \mathbf{0}_3 \; ; \quad \begin{matrix} \alpha = -1, & \beta = 1, & j > i \\ \alpha = 1, & \beta = -1, & j < i \end{matrix}$$

$$\mathbf{A}_{jk}^{(p)} = \begin{bmatrix} 0 & \alpha/l_{jk} & \beta/l_{jk} & & 0 & 0 & 0 \\ \gamma_{jki}^{(p)} & \gamma_{jkj}^{(p)} & \gamma_{jkk}^{(p)} & \mathbf{0}_3 & \gamma_{jkk}^{(b)} & \gamma_{jkj}^{(b)} & \gamma_{jkm}^{(b)} \end{bmatrix} \mathbf{0}_3 \; ; \quad \begin{matrix} \alpha = -1, & \beta = 1, & k > j \\ \alpha = 1 & \beta = -1, & k < j \end{matrix}$$

$$\mathbf{A}_{ki}^{(p)} = \begin{bmatrix} \beta/l_{ki} & 0 & \alpha/l_{ki} & & & 0 & 0 & 0 \\ \gamma_{kii}^{(p)} & \gamma_{kij}^{(p)} & \gamma_{kik}^{(p)} & \mathbf{0}_3 & \mathbf{0}_3 & \gamma_{kii}^{(c)} & \gamma_{kik}^{(c)} & \gamma_{kin}^{(c)} \end{bmatrix} \; ; \quad \begin{matrix} \alpha = 1, & \beta = -1, & k > i \\ \alpha = -1, & \beta = 1, & k < i \end{matrix}$$

$$\gamma_{ijk}^{(p)} = \frac{1}{2} \boldsymbol{\lambda}_{ij}^{(p)} \boldsymbol{\nabla} N_k^{(p)}, \quad \boldsymbol{\lambda}_{ij}^{(p)} = [-s_{ij}^{(p)}, c_{ij}^{(p)}], \quad \mathbf{0}_3 = \begin{bmatrix} 0 & 0 & 0 \\ 0 & 0 & 0 \end{bmatrix}$$

$$\boldsymbol{\nabla} N_k^{(p)} = \begin{bmatrix} \dfrac{\partial N_k}{\partial x'} \\[2mm] \dfrac{\partial N_k}{\partial y'} \end{bmatrix}^{(p)} = \frac{1}{2A^{(p)}} \begin{Bmatrix} b_i \\ c_i \end{Bmatrix}^{(p)} ; \quad b_i^{(p)} = y_j'^{(p)} - y_k'^{(p)}; \quad c_i^{(p)} = x_k'^{(p)} - x_j'^{(p)}$$

Substituting equations (38) and (42) into (37) and choosing a standard linear interpolation for the displacement field within each triangle, the curvatures for the control domain can be expressed in terms of the normal deflection values of patch nodes as

$$\boldsymbol{\kappa}'_p = \mathbf{S}_p \mathbf{w}'_p \tag{44}$$

$$\mathbf{S}_p = [\mathbf{S}_{ij}^{(p)}, \mathbf{S}_{jk}^{(p)}, \mathbf{S}_{ki}^{(p)}] \tag{45}$$

$$\mathbf{w}'_p = [w_i'^{(p)}, w_j'^{(p)}, w_k'^{(p)}, w_j'^{(a)}, w_i'^{(a)}, w_l'^{(a)}, w_k'^{(b)}, w_j'^{(b)}, w_m'^{(b)}, w_i'^{(c)}, w_k'^{(c)}, w_n'^{(c)}]^{\mathrm{T}} \tag{46}$$

The form of the different $\mathbf{S}_{ij}^{(p)}$ matrices is given in Box IV. Note also that the definition of vector $\mathbf{w}'_p$ depends on the convenion chosen for the local and global node numbers for the element patch (Figure 7).

The normal nodal deflections are related to the global nodal displacements by the following transformation:

$$\mathbf{w}'_p = \mathbf{C}_P \mathbf{a}_p \tag{47}$$

where

$$
\mathbf{C}_p = \begin{pmatrix}
i & j & k & l & m & n \\
\mathbf{C}_i^{(p)} & \mathbf{0} & \mathbf{0} & \mathbf{0} & \mathbf{0} & \mathbf{0} \\
\mathbf{0} & \mathbf{C}_i^{(p)} & \mathbf{0} & \mathbf{0} & \mathbf{0} & \mathbf{0} \\
\mathbf{0} & \mathbf{0} & \mathbf{C}_i^{(p)} & \mathbf{0} & \mathbf{0} & \mathbf{0} \\
\mathbf{0} & \mathbf{C}_i^{(a)} & \mathbf{0} & \mathbf{0} & \mathbf{0} & \mathbf{0} \\
\mathbf{C}_i^{(a)} & \mathbf{0} & \mathbf{0} & \mathbf{0} & \mathbf{0} & \mathbf{0} \\
\mathbf{0} & \mathbf{0} & \mathbf{0} & \mathbf{C}_i^{(a)} & \mathbf{0} & \mathbf{0} \\
\mathbf{0} & \mathbf{0} & \mathbf{C}_i^{(b)} & \mathbf{0} & \mathbf{0} & \mathbf{0} \\
\mathbf{0} & \mathbf{C}_i^{(b)} & \mathbf{0} & \mathbf{0} & \mathbf{0} & \mathbf{0} \\
\mathbf{0} & \mathbf{0} & \mathbf{0} & \mathbf{0} & \mathbf{C}_i^{(b)} & \mathbf{0} \\
\mathbf{C}_i^{(c)} & \mathbf{0} & \mathbf{0} & \mathbf{0} & \mathbf{0} & \mathbf{0} \\
\mathbf{0} & \mathbf{0} & \mathbf{C}_i^{(c)} & \mathbf{0} & \mathbf{0} & \mathbf{0} \\
\mathbf{0} & \mathbf{0} & \mathbf{0} & \mathbf{0} & \mathbf{0} & \mathbf{C}_i^{(c)}
\end{pmatrix}, \quad
\mathbf{a}_p = \begin{Bmatrix}
\mathbf{u}_i \\
\mathbf{u}_j \\
\mathbf{u}_k \\
\mathbf{u}_l \\
\mathbf{u}_m \\
\mathbf{u}_n
\end{Bmatrix}
\tag{48}
$$

with

$$
\mathbf{C}_i^{(p)} = [c_{z'x}^{(p)}, c_{z'y}^{(p)}, c_{z'z}^{(p)}], \quad \mathbf{u}_i = \begin{Bmatrix} u_i \\ v_i \\ w_i \end{Bmatrix}
\tag{49}
$$

In the above $c_{z'x}^{(p)}$ is the cosine of the angle between the local z' axis of element p and the global x axis, etc.

Substituting equation (47) into (44) gives finally

$$
\boldsymbol{\kappa}_p' = \mathbf{B}_{b_p} \mathbf{a}_p
\tag{50}
$$

where

$$
\mathbf{B}_{b_p} = \mathbf{S}_p \mathbf{C}_p
\tag{51}
$$

is the curvature matrix of the control pth domain. In equations (47) and (50) $\mathbf{a}_p$ is the vector containing the eighteen nodal displacement variables of the six nodes belonging to the patch of elements associated to the pth control domain. Recall that in the BST element control domains coincide with triangles.

The bending stiffness matrix associated to the pth control domain is obtained by

$$
\mathbf{K}_{b_p} = A^{(p)} \mathbf{B}_{b_p}^{\mathrm{T}} \mathbf{D}_p \mathbf{B}_{b_p}
\tag{52}
$$

where $\mathbf{D}_p$ is the bending constitutive matrix for the patch (see equation (8)).

BST element. Membrane stiffness matrix

The membrane contribution to the BST element is simply provided by the Constant Strain Triangle (CST) under plane stress conditions. The local membrane strains are defined within each

element in terms of the nodal displacements as

$$\boldsymbol{\varepsilon}'_m = \sum_{i=1}^{3} \mathbf{B}'^{(p)}_{m_i}\mathbf{u}'^{(p)}_i = \mathbf{B}'^{(p)}_m\mathbf{a}'^{(p)}_m \tag{53}$$

where

$$\boldsymbol{\varepsilon}'_m = \left[\frac{\partial u'}{\partial x'}, \frac{\partial v'}{\partial y'}, \frac{\partial u'}{\partial y'} + \frac{\partial v'}{\partial x'}\right]^{\mathrm{T}} \tag{54}$$

$$\mathbf{B}'^{(p)}_{m_i} = \begin{bmatrix} \dfrac{\partial N_i^{(p)}}{\partial x'} & 0 \\ 0 & \dfrac{\partial N_i^{(p)}}{\partial y'} \\ \dfrac{\partial N_i^{(p)}}{\partial y'} & \dfrac{\partial N_i^{(p)}}{\partial x'} \end{bmatrix} = \frac{1}{2A^{(p)}}\begin{bmatrix} b_i & 0 \\ 0 & c_i \\ c_i & b_i \end{bmatrix}^{(p)} \tag{55}$$

$$\mathbf{a}'^{(p)}_m = \left\{ \begin{array}{c} \mathbf{u}'^{(p)}_i \\ \mathbf{u}'^{(p)}_j \\ \mathbf{u}'^{(p)}_k \end{array} \right\} \quad \text{and} \quad \mathbf{u}'^{(p)}_i = [u'^{(p)}_i, v'^{(p)}_i]^{\mathrm{T}}$$

In the above $u'^{(p)}_i$ and $v'^{(p)}_i$ are the local in plane displacements along x', y' axis (Figure 8) and $b_i^{(p)}, c_i^{(p)}$ are defined in Box IV.

The membrane strains within a control domain (coinciding with a triangle) are expressed now in terms of the eighteen global nodal displacements of the four elements patch as follows

$$\boldsymbol{\varepsilon}'_m = \mathbf{B}'^{(e)}_m\mathbf{L}_p\mathbf{a}_p = \mathbf{B}_{m_p}\mathbf{a}_p \tag{56}$$

where

$$\mathbf{B}_{m_p} = \mathbf{B}'^{(e)}_m\mathbf{L}_p \tag{57}$$

The transformation matrix $\mathbf{L}_p$ is given by

$$\mathbf{L}_p = \begin{bmatrix} \mathbf{L}^{(p)} & \mathbf{0} & \mathbf{0} \\ \mathbf{0} & \mathbf{L}^{(p)} & \mathbf{0} & \mathbf{0} \\ \mathbf{0} & \mathbf{0} & \mathbf{L}^{(p)} & 6\times 9 \end{bmatrix}, \quad \mathbf{L}^{(p)} = \begin{bmatrix} c_{x'x} & c_{x'y} & c_{x'z} \\ c_{y'x} & c_{y'y} & c_{y'z} \end{bmatrix}^{(p)} \tag{58}$$

The membrane stiffness matrix associated to the pth control domain is obtained as

$$\mathbf{K}_{m_p} = A^{(p)}\mathbf{B}^{\mathrm{T}}_{m_p}\mathbf{D}_m\mathbf{B}_{m_p} \tag{59}$$

where for an isotropic homogeneous material

$$\mathbf{D}_m = \frac{Et}{(1-v^2)}\begin{bmatrix} 1 & v & 0 \\ v & 1 & 0 \\ 0 & 0 & \dfrac{1-v}{2} \end{bmatrix} \tag{60}$$

BST element. Full stiffness matrix and nodal force vector

The stiffness matrix for the BST element is obtained by adding the membrane and bending contributions, i.e.

$$\mathbf{K}_p = \mathbf{K}_{b_p} + \mathbf{K}_{m_p} \tag{61}$$

where $\mathbf{K}_{b_p}$ and $\mathbf{K}_{m_p}$ are given by equations (52) and (59), respectively.

Recall that the dimensions of the stiffness matrix $\mathbf{K}_p$ is 18×18 as it links the eighteen displacements of the six nodes contributing to the control domain. The assembly of the stiffness matrices $\mathbf{K}_p$ into the global equation system follows the standard procedure, i.e. a control domain is treated as a macro-triangular element with six nodes.

The equivalent nodal force vector is obtained similarly as for standard C_0 shell triangular elements. Thus, the contribution of a uniformly distributed load over an element is splitted into three equal parts among the three element nodes. As usual nodal point loads are directly assigned to a node.

Boundary conditions for the BST element

The procedure for prescribing the boundary conditions for the BST element follows the same lines explained for the BPT plate triangle.

The process is simplified as the side rotations are formulated in terms of the normal and tangential values. This allows to treat naturally all boundary condition types found in practice.

Thus, the conditions on the normal rotations are introduced when forming the curvature matrix, whereas the conditions on the nodal displacements and the tangential rotations are prescribed at the solution equation level.

Clamped edge ($\mathbf{u}_i = \mathbf{u}_j = \theta_{n_{ij}} = \theta_{s_{ij}} = 0$)

The condition $\mathbf{u}_i = \mathbf{u}_j = 0$ is prescribed when solving the global system of equations. Note that, the condition $\theta_{s_{ij}} = 0$ is automatically satisfied by prescribing the side displacements to a zero value.

The condition $\theta_{n_{ij}} = 0$ is imposed by making zero the second row of matrix $\mathbf{A}_{ij}^{(p)}$ (see Box IV) as this naturally enforces the condition of zero normal side rotations in equation (42).

Note that the control domain in this case has the element adjacent to the boundary side missing. This has to be properly taken into account in the assembly process.

Simply supported edge ($\mathbf{u}_i = \mathbf{u}_j = \theta_{s_{ij}} = 0$)

This condition is simply imposed by prescribing $\mathbf{u}_i = \mathbf{u}_j = 0$ at the global equation solution level.

Symmetry edge ($\theta_{n_{ij}} = 0$)

The condition of zero normal side rotation is imposed by making zero the second row of matrix $\mathbf{A}_{ij}^{(p)}$ as described above.

Free edge

Matrix $\mathbf{A}_{ij}^{(p)}$ is modified by ignoring the contribution from the missing adjacent element to the boundary side ij. This simply involves making $\gamma_{ijj}^{(a)} = \gamma_{iji}^{(a)} = \gamma_{ijl}^{(a)} = 0$ and changing the $1/2$ in the definition of $\gamma_{ijk}^{(p)}$ to a unit value (see Box IV).
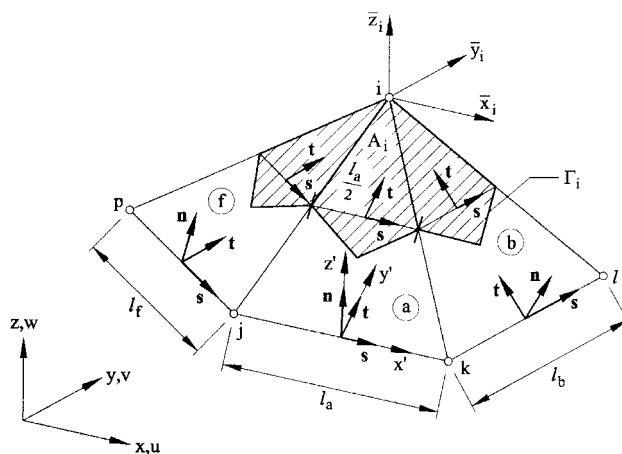
Figure 10. BSN element. Control domain and coordinate systems

BASIC SHELL NODAL ELEMENT (BSN)

The BPN plate element described in a previous section is extended now to shell analysis. The derivation of the bending and membrane stiffness matrices is described next.

BSN element. Bending stiffness matrix

Figure 10 shows a typical *vertex centred* control domain surrounding a node and the corresponding patch of BPN shell triangles. The following co-ordinate systems are defined:

Global system: x, y, z, defining the global displacements u, v, w.

Local element system: x', y', z', defining the element curvatures. Vector x' is defined along the direction of the external side of each element in the patch, z' is the normal direction to the element and the y' axis is obtained by cross product of unit vectors along the z' and x' directions.

Nodal system: $\bar{x}, \bar{y}, \bar{z}$, defining the constant curvatures field over the control domain. Here $\bar{z}$ is the average normal direction at the node, $\bar{x}$ is defined as orthogonal to $\bar{z}$ and lying on the global plane x, z (if $\bar{z}$ coincides with the global y axis, then $\bar{x} = z$) and the $\bar{y}$ direction is taken as cross product of unit vectors in the $\bar{z}$ and $\bar{x}$ directions.

A constant curvatures field is defined over each control domain. For convenience the curvatures are defined in the nodal co-ordinate system. From simple transformation rules for each triangular element we can write

$$\bar{\boldsymbol{\kappa}} = \mathbf{R}_1 \boldsymbol{\kappa} = \mathbf{R}_1 \mathbf{R}_2 \boldsymbol{\kappa}' \tag{62}$$

In the above

$$\bar{\boldsymbol{\kappa}} = \left[-\frac{\partial^2 \bar{w}}{\partial \bar{x}^2}, -\frac{\partial^2 \bar{w}}{\partial \bar{y}^2}, -2\frac{\partial^2 \bar{w}}{\partial \bar{x} \partial \bar{y}} \right]^{\mathrm{T}} \tag{63}$$

is the nodal curvature vector

$$\boldsymbol{\kappa}' = \left[-\frac{\partial^2 w'}{\partial x'^2}, -\frac{\partial^2 w'}{\partial y'^2}, -2\frac{\partial^2 w'}{\partial x' \partial y'} \right]^{\mathrm{T}} \tag{64}$$

is the element curvature vector and $\boldsymbol{\kappa}$ is an auxiliary 'global' curvature vector used to simplify the transformation from element to nodal (local) curvatures. Recall that w' is the deflection in the direction of the z' axis. The transformation matrices $\mathbf{R}_1$ and $\mathbf{R}_2$ are given by

$$\mathbf{R}_1 = \begin{bmatrix} c_{\bar{x}x}^2 & c_{\bar{x}y}^2 & c_{\bar{x}z}^2 & c_{\bar{x}x}c_{\bar{x}y} & c_{\bar{x}x}c_{\bar{x}z} & c_{\bar{x}y}c_{\bar{x}z} \\ c_{\bar{y}x}^2 & c_{\bar{y}y}^2 & c_{\bar{y}z}^2 & c_{\bar{y}x}c_{\bar{y}y} & c_{\bar{y}x}c_{\bar{y}z} & c_{\bar{y}y}c_{\bar{y}z} \\ 2c_{\bar{x}x}2c_{\bar{y}x} & 2c_{\bar{x}y}c_{\bar{y}y} & 2c_{\bar{x}z}c_{\bar{y}z} & c_{\bar{x}y}c_{\bar{y}x} + c_{\bar{x}x}c_{\bar{y}y} & c_{\bar{x}z}c_{\bar{y}x} + c_{\bar{x}x}c_{\bar{y}z} & c_{\bar{x}z}c_{\bar{y}y} + c_{\bar{x}y}c_{\bar{y}z} \end{bmatrix} \tag{65}$$

$$\mathbf{R}_2 = \begin{bmatrix} c_{x'x}^2 & c_{y'x}^2 & c_{x'x}c_{y'x} \\ c_{x'y}^2 & c_{y'y}^2 & c_{x'y}c_{y'y} \\ c_{x'z}^2 & c_{y'z}^2 & c_{x'z}c_{y'z} \\ 2c_{x'x}c_{x'y} & 2c_{y'x}c_{y'y} & c_{x'y}c_{y'x} + c_{x'x}c_{y'y} \\ 2c_{x'x}c_{x'z} & 2c_{y'x}c_{y'z} & c_{x'z}c_{y'x} + c_{x'x}c_{y'z} \\ 2c_{x'y}c_{x'z} & 2c_{y'y}c_{y'z} & c_{x'z}c_{y'y} + c_{x'y}c_{y'z} \end{bmatrix} \tag{66}$$

where as usual $c_{\bar{x}x}$ is the cosine of the angle between $\bar{x}$ and x axes, etc.

Let us write equation (62) in integral form using the weighted residual method with unit weight functions [1] as

$$\int_{A_i} [\bar{\boldsymbol{\kappa}} - \mathbf{R}_1\mathbf{R}_2\boldsymbol{\kappa}'] \mathrm{d}A = 0 \tag{67}$$

where A_i is the area of the ith control domain surrounding node i. A simple integration by parts gives (noting that the curvatures $\bar{\boldsymbol{\kappa}}$ and the transformation matrix $\mathbf{R}_1$ are constant within the control domain)

$$\bar{\boldsymbol{\kappa}}_i = \frac{1}{A_i}\mathbf{R}_1^{(i)} \int_{\Gamma_i} \mathbf{R}_2\mathbf{T}\boldsymbol{\nabla}'w' \, \mathrm{d}\Gamma \tag{68}$$

where $\mathbf{T}$ is given by equation (36b). In the derivation of equation (68) the changes of the transformation matrix $\mathbf{R}_2$ across the element sides have been neglected. Note that these changes tend to zero as the mesh is refined.

Equation (68) can be computed by performing the boundary integral over the different elements which contribute to the control domain of node i, i.e.

$$\bar{\boldsymbol{\kappa}}_i = \frac{1}{A_i}\mathbf{R}_1^{(i)} \sum_j \frac{l_j}{2}\mathbf{R}_2^{(j)}\mathbf{T}_j\boldsymbol{\nabla}'w' \tag{69}$$

where the sum extends over the number of elements contributing to the ith control domain, l_j is the external side of element j (see Figure 10) and A_i is the area of the ith control domain $A_i = \frac{1}{3}\sum_{j=1}^{n_i} A_j^{(i)}$, where $A_j^{(i)}$ is the area of the jth triangular element contributing to the control domain.

Substituting in equation (69) the standard linear interpolation for the normal deflection w' within each triangle gives

$$\bar{\boldsymbol{\kappa}}_i = \mathbf{S}_i \mathbf{w}'_i \tag{70}$$

with

$$
\begin{array}{cccc}
1 & 2 & \ldots & n_i
\end{array}
$$
$$\mathbf{S}_i = \left[\mathbf{S}_i^{(a)}, \mathbf{S}_i^{(b)}, \ldots, \mathbf{S}_i^{(r)} \right] \tag{71}$$

where n_i is the number of elements in the ith patch (for instance $n_i = 6$ in the patch shown in Box V) and superindexes $a, b, \ldots, r$ refer to global element numbers. Matrix $\mathbf{S}_i^{(k)}$ is given by

$$\mathbf{S}_i^{(k)} = \mathbf{F}_i^{(k)} \left[\mathbf{G}_1^{(k)}, \mathbf{G}_2^{(k)}, \mathbf{G}_3^{(k)} \right] \tag{72}$$

with

$$\mathbf{F}_i^{(k)} = \frac{l_k}{2A_i} \mathbf{R}_1^{(i)} \mathbf{R}_2^{(k)} \mathbf{T}_k \tag{73}$$

and

$$\mathbf{G}_i^{(k)} = \boldsymbol{\nabla}' N_i^{(k)} = \frac{1}{2A^{(k)}} \left\{ \begin{array}{c} b_i^{(k)} \\ c_i^{(k)} \end{array} \right\}, \quad b_i^{(k)} = x_j'^{(k)} - x_k'^{(k)}, \quad c_i^{(k)} = y_k'^{(k)} - y_j'^{(k)} \tag{74}$$

Vector $\mathbf{w}'_i$ is given by

$$\mathbf{w}'_i = \left\{ \begin{array}{c} \mathbf{w}'^{(a)} \\ \mathbf{w}'^{(b)} \\ \vdots \\ \mathbf{w}'^{(r)} \end{array} \right\} \begin{array}{c} 1 \\ 2 \\ \\ p_n \end{array}, \quad \mathbf{w}'^{(k)} = [w_1'^{(k)}, w_2'^{(k)}, w_3'^{(k)}]^{\mathrm{T}} \tag{75}$$

The final step is to transform the local nodal deflection vector $\mathbf{w}'_i$ to global axes. The process follows the transformations explained for the BST element (see equations (47)–(49)), i.e.

$$\mathbf{w}'_i = \mathbf{C}_i \mathbf{a}_i \tag{76}$$

with

$$\mathbf{a}_i^{\mathrm{T}} = \left[\mathbf{u}_i^{\mathrm{T}}, \mathbf{u}_j^{\mathrm{T}}, \mathbf{u}_k^{\mathrm{T}}, \ldots, \mathbf{u}_{p_n}^{\mathrm{T}} \right], \quad \mathbf{u}_i = [u_i, v_i, w_i]^{\mathrm{T}} \tag{77}$$

In equations (75) and (77) p_n is the number of nodes in the patch linked to the ith control domain (i.e. $p_n = 7$ for the patch shown in Box V).

The form of the transformation matrix $\mathbf{C}_i$ depends naturally on the numbering of nodes in the patch. A simple numbering scheme can be derived by taking the central node as the first node for each element and the remaining two edge nodes in anticlockwise order as nodes 2 and 3. An example of this numbering scheme is shown in Box V.

The curvature matrix is finally obtained by substituting equation (76) into (70) giving

$$\bar{\boldsymbol{\kappa}}_i = \mathbf{B}_{b_i} \mathbf{a}_i \tag{78}$$

Box V. Example of computation of the curvature matrix for the BSN element

$$\bar{\boldsymbol{\kappa}}_i = \mathbf{S}_i \mathbf{w}_i' \qquad \mathbf{S}_i = [\mathbf{S}_i^{(a)}, \mathbf{S}_i^{(b)}, \mathbf{S}_i^{(c)}, \mathbf{S}_i^{(d)}, \mathbf{S}_i^{(e)}, \mathbf{S}_i^{(f)}], \qquad \mathbf{S}_i^{(k)} = \mathbf{F}_i^{(k)}[\mathbf{G}_1^{(k)}, \mathbf{G}_2^{(k)}, \mathbf{G}_3^{(k)}]$$

$$\mathbf{F}_i^{(k)} = \frac{l_k}{2A_i} \mathbf{R}_1^{(i)} \mathbf{R}_2^{(k)'} \mathbf{T}_k, \qquad \mathbf{G}_i^{(k)} = \boldsymbol{\nabla}' N_i^{(k)} = \frac{1}{2A^{(k)}} \left\{ \begin{array}{c} b_i^{(k)} \\ c_i^{(k)} \end{array} \right\},$$

$$b_i^{(k)} = x_j'^{(k)} - x_k'^{(k)}, \ \ c_i^{(k)} = y_k'^{(k)} - y_j'^{(k)}$$

$$w_i' = \left[w_i'^{(a)}, w_j'^{(a)}, w_k'^{(a)}, w_i'^{(b)}, w_k'^{(b)}, w_l'^{(b)}, w_i'^{(c)}, w_l'^{(c)}, w_m'^{(c)}, w_i'^{(d)}, w_m'^{(d)}, w_n'^{(d)}, \right.$$
$$\left. w_i'^{(e)}, w_n'^{(e)}, w_p'^{(e)}, w_i'^{(f)}, w_p'^{(f)}, w_j'^{(f)} \right]^{\mathrm{T}}$$

$$\mathbf{w}_i' = \mathbf{C}_i \mathbf{a}_i \Rightarrow \boxed{\bar{\boldsymbol{\kappa}}_i = \mathbf{S}_i \mathbf{C}_i \mathbf{a}_i = \mathbf{B}_i \mathbf{a}_i}$$

$$
\mathbf{C}_i = \begin{pmatrix}
\mathbf{C}_i^{(a)} & 0 & 0 & 0 & 0 & 0 & 0 \\
0 & \mathbf{C}_j^{(a)} & 0 & 0 & 0 & 0 & 0 \\
0 & 0 & \mathbf{C}_k^{(a)} & 0 & 0 & 0 & 0 \\
\mathbf{C}_i^{(b)} & 0 & 0 & 0 & 0 & 0 & 0 \\
0 & 0 & \mathbf{C}_k^{(b)} & 0 & 0 & 0 & 0 \\
0 & 0 & 0 & \mathbf{C}_l^{(b)} & 0 & 0 & 0 \\
\mathbf{C}_i^{(c)} & 0 & 0 & 0 & 0 & 0 & 0 \\
0 & 0 & 0 & \mathbf{C}_l^{(c)} & 0 & 0 & 0 \\
0 & 0 & 0 & 0 & \mathbf{C}_m^{(c)} & 0 & 0 \\
\mathbf{C}_i^{(d)} & 0 & 0 & 0 & 0 & 0 & 0 \\
0 & 0 & 0 & 0 & \mathbf{C}_m^{(d)} & 0 & 0 \\
0 & 0 & 0 & 0 & 0 & \mathbf{C}_n^{(d)} & 0 \\
\mathbf{C}_i^{(e)} & 0 & 0 & 0 & 0 & 0 & 0 \\
0 & 0 & 0 & 0 & 0 & \mathbf{C}_n^{(e)} & 0 \\
0 & 0 & 0 & 0 & 0 & 0 & \mathbf{C}_p^{(e)} \\
\mathbf{C}_i^{(f)} & 0 & 0 & 0 & 0 & 0 & 0 \\
0 & 0 & 0 & 0 & 0 & 0 & \mathbf{C}_p^{(f)} \\
0 & \mathbf{C}_j^{(f)} & 0 & 0 & 0 & 0 & 0
\end{pmatrix}, \quad
\mathbf{a}_i = \left\{ \begin{array}{c} \mathbf{u}_i \\ \mathbf{u}_j \\ \mathbf{u}_k \\ \mathbf{u}_l \\ \mathbf{u}_m \\ \mathbf{u}_n \\ \mathbf{u}_p \end{array} \right\}, \quad
\mathbf{u}_i = \left\{ \begin{array}{c} u_i \\ v_i \\ w_i \end{array} \right\}
$$

with column headers $i \quad j \quad k \quad l \quad m \quad n \quad p$

with the curvature matrix given for the ith control domain given by

$$\mathbf{B}_{b_i} = \mathbf{S}_i \mathbf{C}_i \tag{79}$$

The bending stiffness matrix for the ith control domain is finally obtained by

$$\mathbf{K}_{b_i} = A_i \mathbf{B}_{b_i}^{\mathrm{T}} \mathbf{D}_i \mathbf{B}_{b_i} \tag{80}$$

where $\mathbf{D}_i$ is given by equation (8b).

Box V shows an example of computation of the curvature matrix for a typical BSN element.

BSN element. Membrane stiffness matrix

The membrane contribution to the BSN element can be obtained from the stiffness matrix of the CST element following the lines explained for the Basic Shell Triangle (BST) in previous section. A difficulty however arises in the assembly of the bending and membrane stiffnesses in this case as cell vertex control domains do not coincide with triangles as in the BST element. This assembly is however possible by identifying the membrane stiffness contribution to each nodal control domain.

An alternative and simpler assembly scheme can be devised by obtaining *directly* the membrane stiffness matrix for each control domain following a similar procedure as for the bending case.

For this purpose a constant membrane field $\bar{\boldsymbol{\varepsilon}}_{\mathrm{m}}$ is assumed over the control domain. For convenience the membrane field $\bar{\boldsymbol{\varepsilon}}_{\mathrm{m}}$ is defined in the nodal co-ordinate system. The relationship between nodal and element membrane strains can be obtained from

$$\bar{\boldsymbol{\varepsilon}}_{\mathrm{m}} = \mathbf{R}_1 \mathbf{R}_2 \boldsymbol{\varepsilon}'_{\mathrm{m}} \tag{81}$$

where $\mathbf{R}_1$ and $\mathbf{R}_2$ are the transformation matrices given by equations (65) and (66) and

$$\bar{\boldsymbol{\varepsilon}}_{\mathrm{m}} = \left[\frac{\partial \bar{u}}{\partial \bar{x}}, \frac{\partial \bar{v}}{\partial \bar{y}}, \frac{\partial \bar{u}}{\partial \bar{y}} + \frac{\partial \bar{v}}{\partial \bar{x}} \right]^{\mathrm{T}} \tag{82a}$$

$$\boldsymbol{\varepsilon}'_{\mathrm{m}} = \left[\frac{\partial u'}{\partial x'}, \frac{\partial v'}{\partial y'}, \frac{\partial u'}{\partial y'} + \frac{\partial v'}{\partial x'} \right]^{\mathrm{T}} \tag{82b}$$

From equation (81) the following expression for the membrane strains in the ith control domain is readily obtained

$$\bar{\boldsymbol{\varepsilon}}_{m_i} = \frac{1}{A_i} \mathbf{R}_1^{(i)} \iint_{A_i} \mathbf{R}_2 \boldsymbol{\varepsilon}'_{\mathrm{m}} \, \mathrm{d}A = \frac{1}{A_i} \mathbf{R}_1^{(i)} \sum_j \frac{A^{(j)}}{3} \mathbf{R}_2^{(j)} \boldsymbol{\varepsilon}_{\mathrm{m}}^{\prime(j)} \tag{83}$$

where the sum extends over the elements contributing to the ith control domain, $\boldsymbol{\varepsilon}_m^{\prime(j)}$ are the local strains over the jth triangular element, $A^{(j)}$ is the area of this triangle and the rest of the terms have the same meaning as in equation (69). Note that in the derivation of equation (83) the local strain field $\boldsymbol{\varepsilon}'_{\mathrm{m}}$ has assumed to be constant over each element in the patch.

The local membrane strains within each element are now readily expressed in terms of the nodal displacements by equation (53). Substituting this equation into (83) the following matrix expression can be found

$$\bar{\boldsymbol{\varepsilon}}_{m_i} = \mathbf{B}'_{m_i} \mathbf{u}'_i \tag{84}$$

where

$$1 \quad 2 \quad \cdots \quad n_i$$
$$\mathbf{B}'_{m_i} = \left[\mathbf{M}_i^{(a)}, \mathbf{M}_i^{(b)}, \ldots, \mathbf{M}_i^{(r)}\right] \tag{85}$$

with

$$\mathbf{M}_i^{(k)} = \mathbf{H}_i^{(k)} \left[\mathbf{B}'^{(k)}_{m_1}, \mathbf{B}'^{(k)}_{m_2}, \mathbf{B}'^{(k)}_{m_3}\right] \tag{86a}$$

$$\mathbf{H}_i^{(k)} = \frac{A^{(k)}}{3A_i} \mathbf{R}_1^{(i)} \mathbf{R}_2^{(k)} \tag{86b}$$

and the expression of $\mathbf{B}'^{(k)}_{m_i}$ is given by equation (55).

In equation (84) $\mathbf{u}_i'^{(k)}$ is the vector of nodal in-plane displacements for each element in the patch given by

$$\mathbf{u}_i' = \left\{\begin{array}{c}\mathbf{u}'^{(a)} \\ \mathbf{u}'^{(b)} \\ \vdots \\ \mathbf{u}'^{(r)}\end{array}\right\}\begin{array}{c}1 \\ 2 \\ \vdots \\ n_i\end{array}, \quad \mathbf{u}'^{(a)} = \left\{\begin{array}{c}\mathbf{u}_1'^{(a)} \\ \mathbf{u}_2'^{(a)} \\ \mathbf{u}_3'^{(a)}\end{array}\right\} \quad \text{with} \quad \mathbf{u}_j'^{(a)} = \left\{\begin{array}{c}u_j'^{(a)} \\ v_j'^{(a)}\end{array}\right\} \tag{87}$$

The next step is to transform vector $\mathbf{u}_i'$ to global axes. The transformation reads

$$\mathbf{u}_i' = \mathbf{L}_i \mathbf{a}_i \tag{88}$$

where $\mathbf{a}_i$ is the global nodal displacement vector for the ith control domain given by equation (77) and $\mathbf{L}_i$ is the local–global transformation matrix. This matrix is obtained by assembling the nodal contributions $\mathbf{L}^{(e)}$ given by equation (58). The structure of $\mathbf{L}_i$ is identical to that of matrix $\mathbf{C}_i$ (see Box V).

Substitution of equation (88) into (84) gives

$$\bar{\boldsymbol{\varepsilon}}_{m_i} = \mathbf{B}'_{m_i} \mathbf{L}_i \mathbf{a}_i = \mathbf{B}_{m_i} \mathbf{a}_i \tag{89}$$

with

$$\mathbf{B}_{m_i} = \mathbf{B}'_{m_i} \mathbf{L}_i \tag{90}$$

The membrane stiffness matrix for the ith control domain is finally given by

$$\mathbf{K}_{m_i} = A_i \mathbf{B}_{m_i}^{\mathrm{T}} \mathbf{D}_{m_i} \mathbf{B}_{m_i} \tag{91}$$

where $\mathbf{D}_{m_i}$ is given by equations (60) and (8b).

BSN element. Full stiffness matrix and nodal force vector

The stiffness matrix for a control domain characterizing a control domain for the BSN element is obtained by adding the membrane and bending contributions as

$$\mathbf{K}_i = \mathbf{K}_{b_i} + \mathbf{K}_{m_i} \tag{92}$$

where $\mathbf{K}_{b_i}$ and $\mathbf{K}_{m_i}$ are given by equations (80) and (90), respectively.

Recall that in the BSN formulation control domains do not coincide with individual elements as in the BST case. The stiffness matrix $\mathbf{K}_i$ of equation (91) assembles all the contributions to a single node and therefore it is already a *global stiffness matrix*. The stiffness assembly process is therefore not necessary as in the case of the BPN element.

The equivalent nodal force vector for the BSN element can be obtained in identical form as for the BST element, i.e. a uniformly distributed load is splitted into three equal parts and assigned to each element node and nodal point loads are directly assigned to the node at global level.

Boundary conditions for the BSN element

The conditions of prescribed displacements are imposed as usual at the equation solution level after the global assembly process.

The conditions on prescribed rotations at edges follow a process similar to that explained for the BPN plate element. Thus, free boundary edges are naturally modelled simply by noting that the free boundary edge is now part of the control domain boundary (see Figure 6). On the other hand the condition of zero rotation along an edge is imposed when forming the curvature matrix by making zero the appropriate row in matrix $\mathbf{G}_j^{(k)}$ of equation (74).

It is worth noting that the nodal definition of curvatures and membrane strains allows to impose the conditions of zero bending and/or axial forces at free and simply supported boundaries by making zero the appropriate rows of the constitutive matrix as explained for the BPN element.

EXAMPLES

Square plates under uniform and point loads

A number of examples of thin square plates have been studied to test the efficiency of the BPT, BPT1 and BPN rotation free plate elements. The examples analysed are the following:

- Simple supported square plate under uniform load (Figure 12)
- Simple supported square plate under central point load (Figure 13)
- Clamped square plate under uniform load (Figure 14)
- Clamped square plate under central point load (Figure 15)

Figure 11 shows the geometry of the plate and the material properties. Results shown in Figures 12–15 have been obtained for structured meshes using the two different mesh orientations shown in Figure 11. Numerical results for the central deflection obtained with the BPT, BPT1 and BPN elements are compared with the standard thin plate solutions [4] and with results obtained with the standard 9 d.o.f. DKT plate element [7, 16] and the 6 d.o.f. Morley plate triangle [6]. Results obtained with the new rotation free plate triangles compare very favourably with those obtained with the DKT element. As expected, the Morley triangle yielded a higher error for the same degrees of freedom in all cases due to the presence of mid-side normal rotations. This substantially increases the numbers of nodal variables in the Morley triangle for the same type of meshes.

Note also that the BPN gave in most cases more accurate results than the BPT and BPT1 elements. However, a good feature of these two elements is that they seem to be insensitive to mesh orientation, a property not shared by the BPN and the DKT triangles.
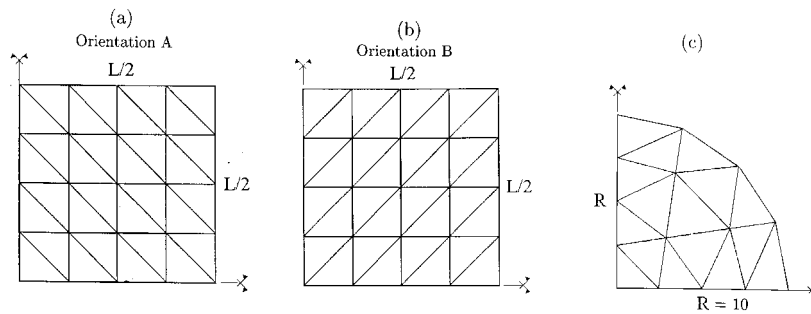
Figure 11. (a) square plate: $L = 10$, structured mesh, orientation A; (b) square plate: structured mesh, orientation B; (c) circular plate: structured mesh. $E = 10 \cdot 92, v = 0 \cdot 3$ and $t = 0 \cdot 01$ in all cases

Note that results for the BPT and BPT1 elements are identical in both cases as expected for regular meshes.

The performance of the new rotation free triangles in non-structured meshes was also found to be remarkable [38]. Results for the central deflection for a clamped plate under a central point load using a non-structured mesh are shown in Figure 16(a).

Circular plates under uniform and central point loads

Figure 11(c) shows the geometry of the plate and the material properties. Again a number of tests using the BPT, BPT1 and BPN rotation free plate triangles was performed using structured and non-structured meshes.

Numerical results for the central deflection using structured meshes are shown in Figures 17 and 18 for the following cases:

(1) Simple supported circular plate under uniform load and a central point load (Figure 17);
(2) Clamped circular plate under a uniform load and a central point load (Figure 18).

The performance of the three rotation free plate elements is excellent. Numerical results were in all cases (with exception of the example of Figure 17(a)) more accurate than those provided by the DKT and the Morley triangles.

Note that results for the BPT and BPT1 differ slightly in this case as the mesh is not regular. No particular trend in the comparison between the results obtained with the two elements is observed. This favours the use of the BPT element for practical purposes due to its simplicity.

Again the performance of all rotation-free plate elements for non-structured meshes was found to be excellent [38]. A typical example is shown in Figure 16(b).

Skew thin plates under uniform load

Figure 19 shows the typical geometry of the skew plates analysed and the material properties. The following cases are considered.

(1) Bi-clamped 30° skewed plate under uniform load (Figure 20)
(2) 60°, 40° and 20° cantilever skewed plates under uniform load (Figures 21–23).
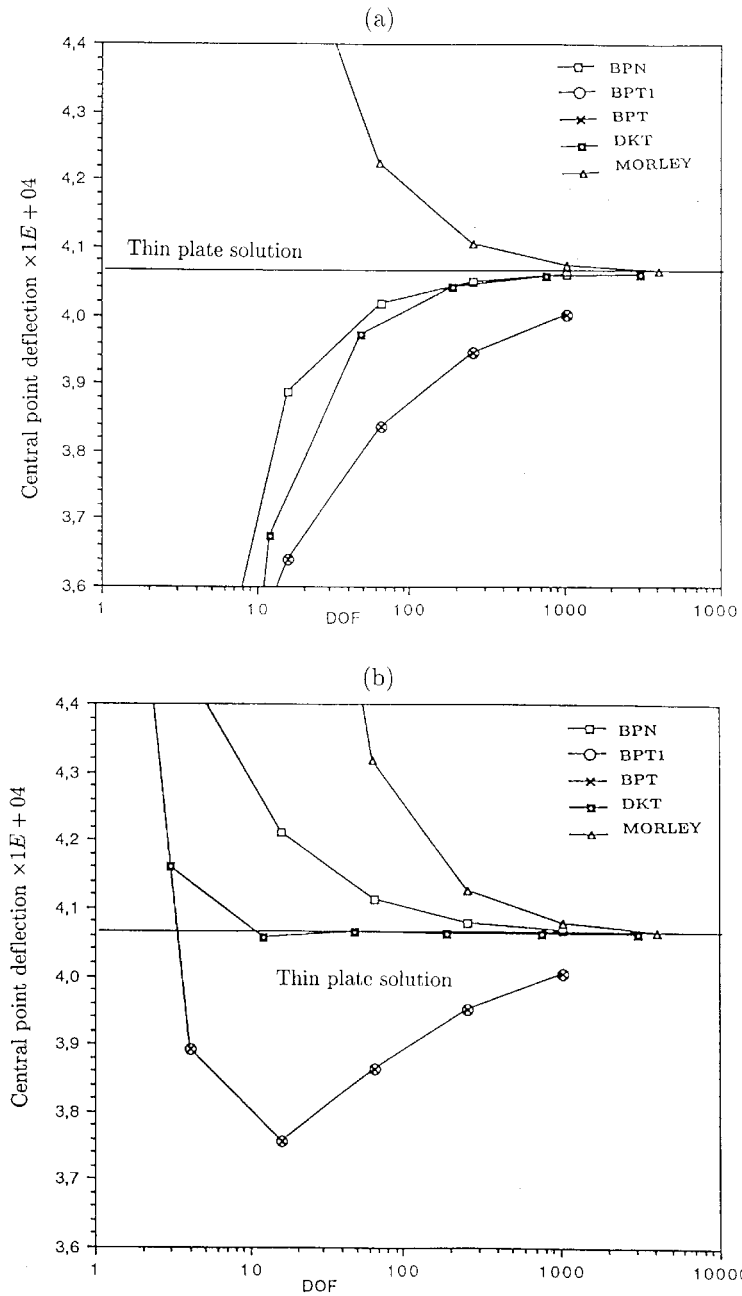
Figure 12. Central point deflection of a simple supported square plate under uniform load: (a) mesh orientation *A*; (b) mesh orientation *B*
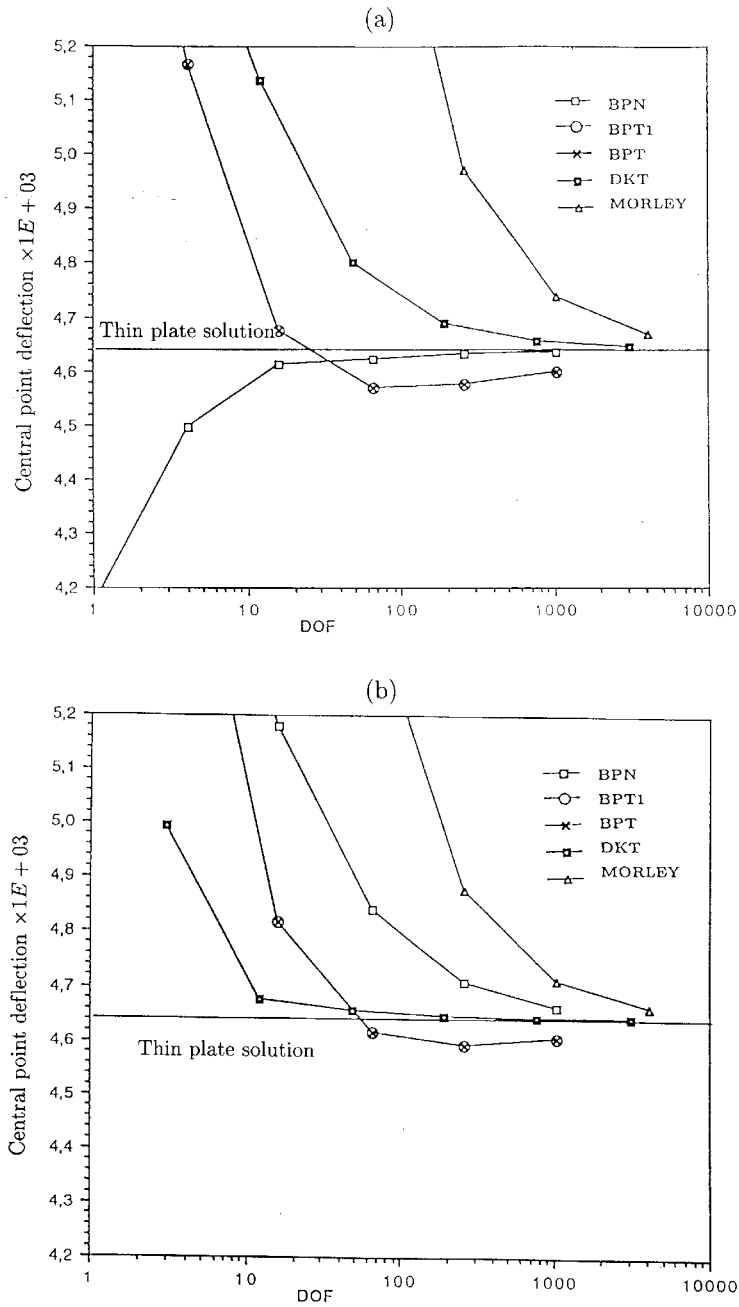
Figure 13. Central point deflection of a simple supported square plate under central point load: (a) mesh orientation *A*, (b) mesh orientation *B*
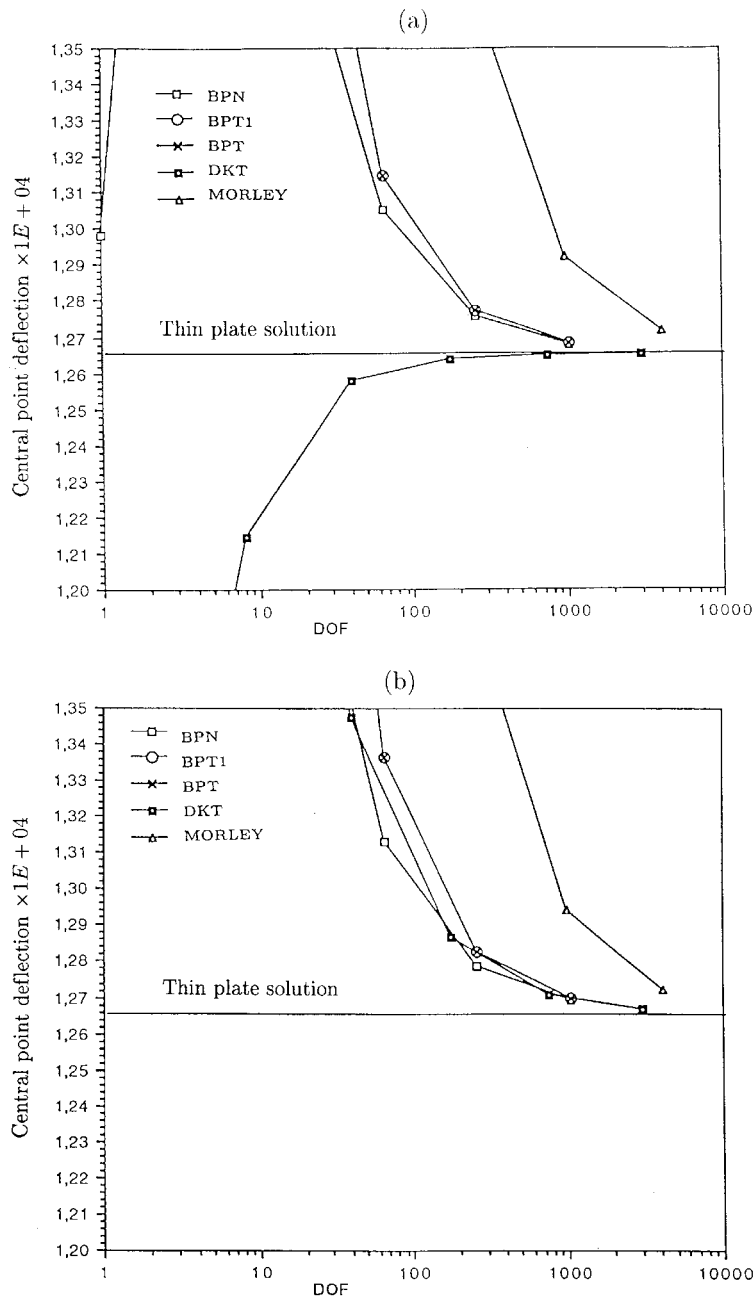
Figure 14. Central point deflection of a clamped square plate under uniform load: (a) mesh orientation *A*; (b) mesh orientation *B*
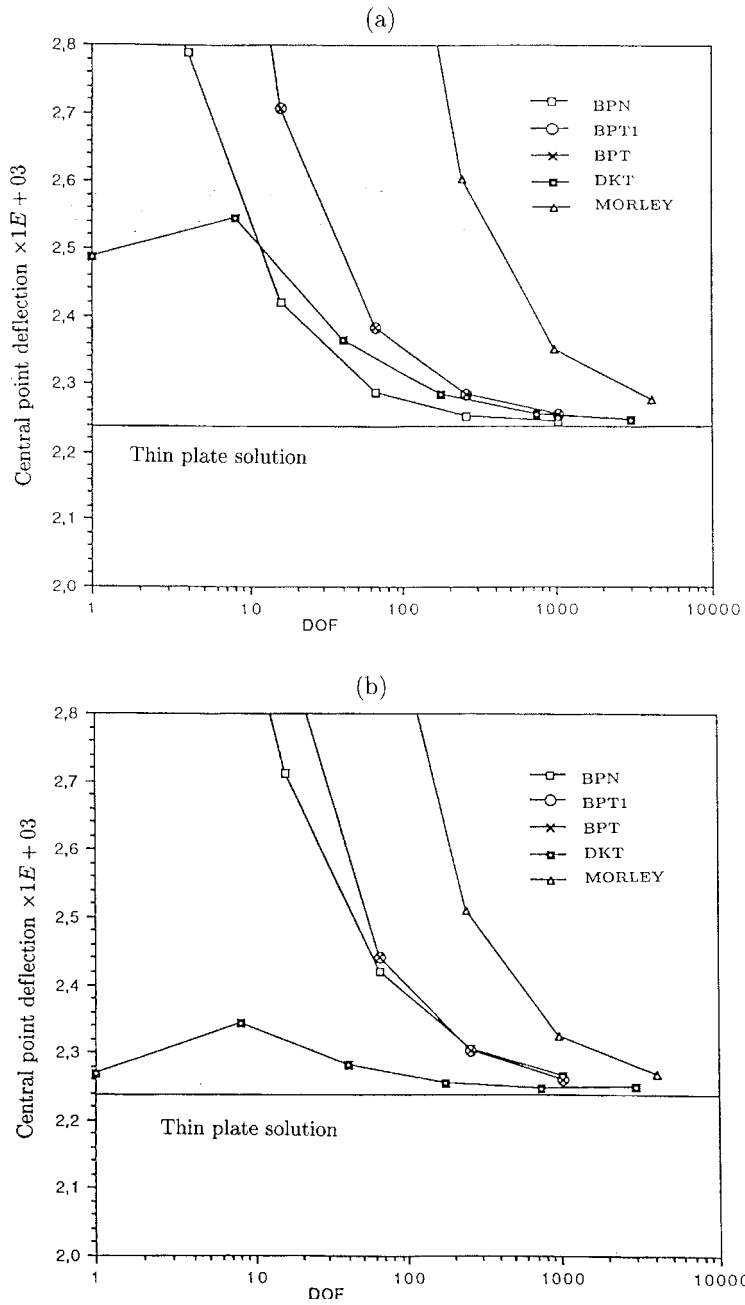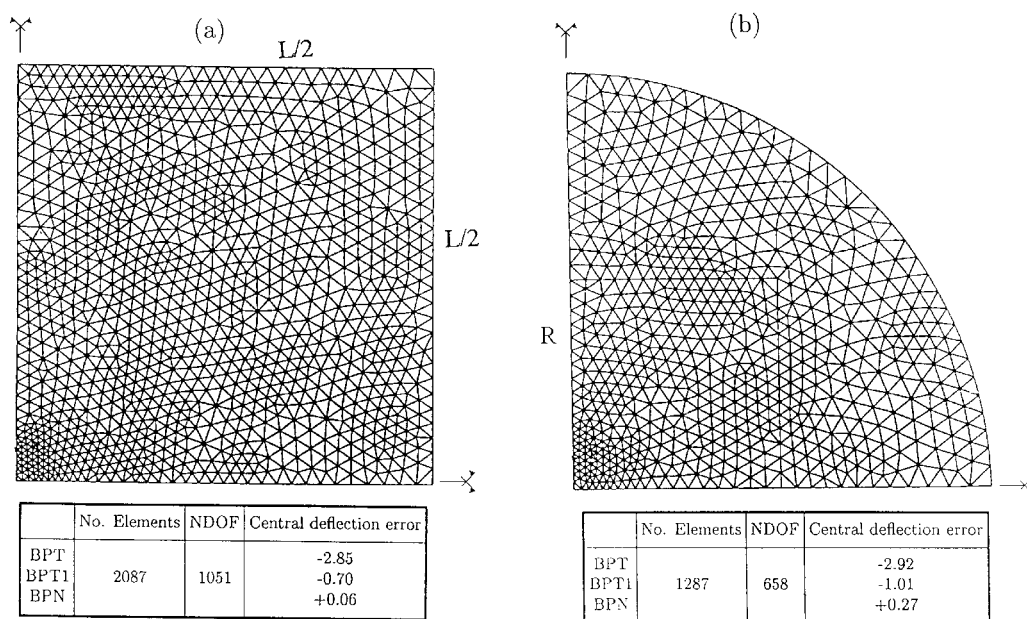
Int. J. Numer. Meth. Engng. **47**, 557–603 (2000)

Figure 15. Central point deflection of a clamped square plate under central point load: (a) mesh orientation *A*; (b) mesh orientation *B*

	No. Elements	NDOF	Central deflection error
BPT			-2.85
BPT1	2087	1051	-0.70
BPN			+0.06

	No. Elements	NDOF	Central deflection error
BPT			-2.92
BPT1	1287	658	-1.01
BPN			+0.27

Figure 16. Central point deflection of clamped square and circular plates under a central point load. Percentage error in central deflection values obtained with BPT, BPT1 and BPN elements using the non-structured meshes shown. Geometry and material properties as in Figure 11

Numerical results obtained with BPT, BPT1, BPN, DKT and Morley triangles using structured meshes are compared with a finite difference solution reported in [39] and with finite element solutions obtained with the DRM and ELM1 Reissner–Mindlin triangles [13, 20] (Figures 21–23).

The performance of the new rotation-free plate elements is also good in all these examples. The maximum error for a 1000 d.o.f. mesh did not exceed 2·5 per cent in all cases. Obviously the solution can be improved using mesh adaptivity as shown in [38].

Cylindrical shell under central point load

Figure 24 shows the geometry of the shell, the material properties and the loading. The problem has been studied with the BST and BSN rotation-free shell triangles using structured and non-structured meshes [38].

Figure 24 shows the convergence of the central deflection obtained using structured meshes. The reference solutions were obtained from [40, 41]. Numerical results for the three rotation-free shell triangles compare well with those obtained with the DKT-15 [7, 16] element also shown.

A plot of the distribution of the bending moment $M_{y'}$ along the central edge AB is shown in Figure 25.

Cylindrical shell under uniform load

The geometry of the dome known Scordelis–Lo shell [42, 43] is shown in Figure 26. The convergence of numerical results for the vertical displacement of the free point B using structured
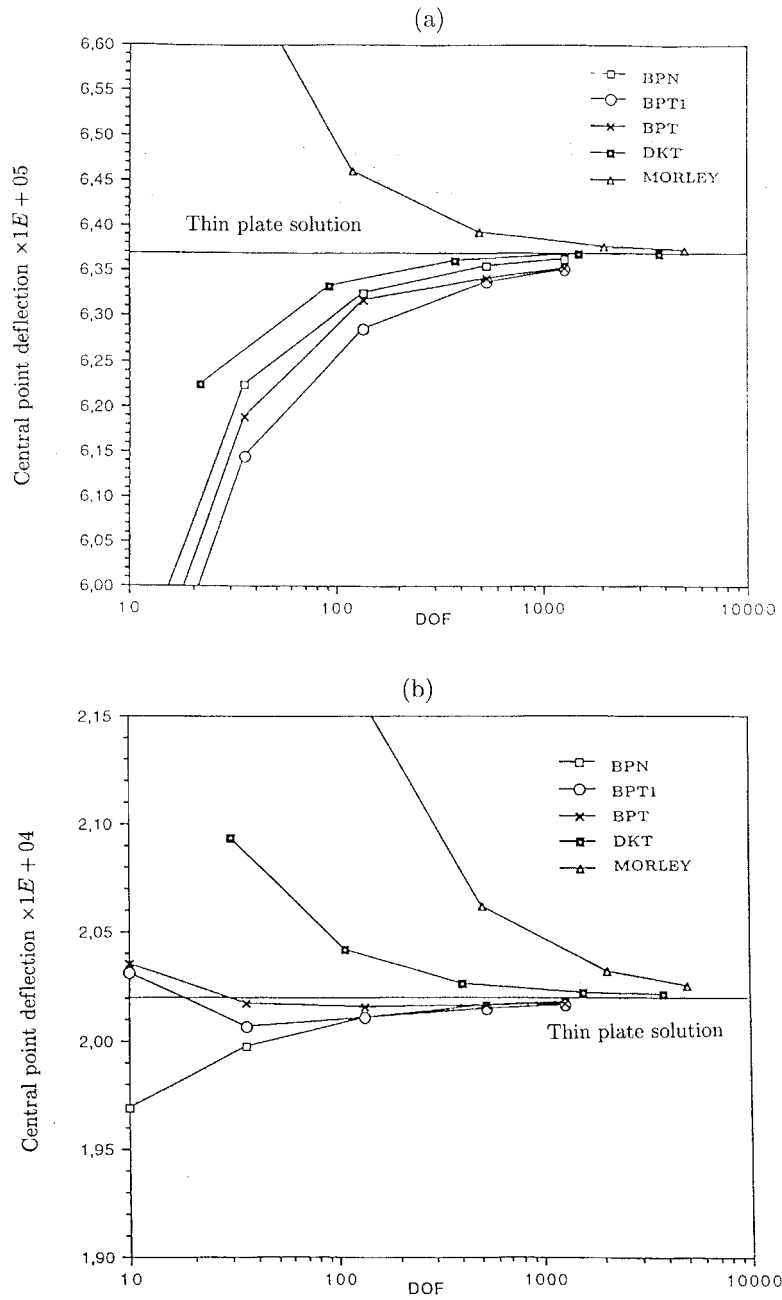
Figure 17. Central point deflection of a simple supported circular plate: (a) Uniform load, (b) central point load
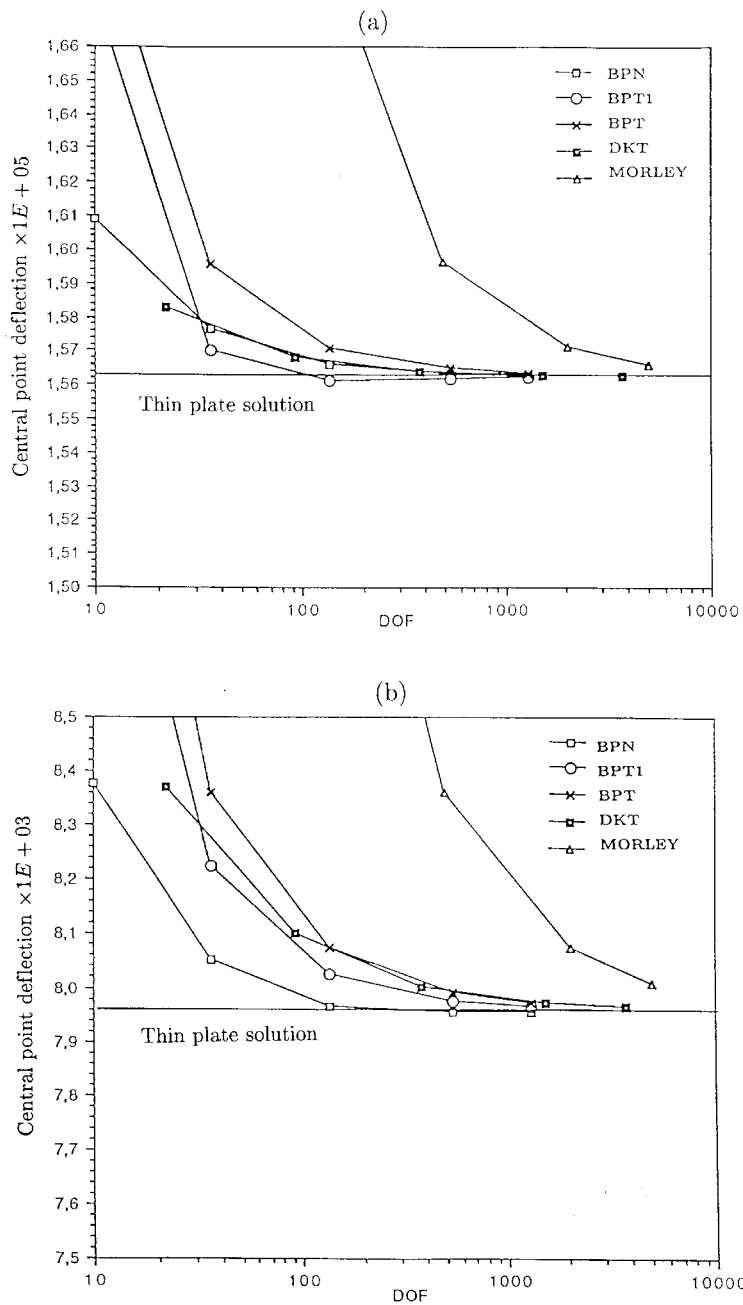
Figure 18. Central point deflection of a clamped circular plate: (a) Uniform load; (b) central point load
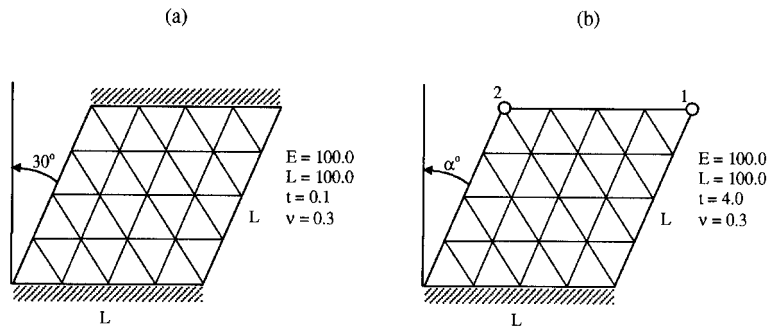
Figure 19. (a) Bi-clamped skewed plate under uniform load; (b) skew cantilever plates under uniform load
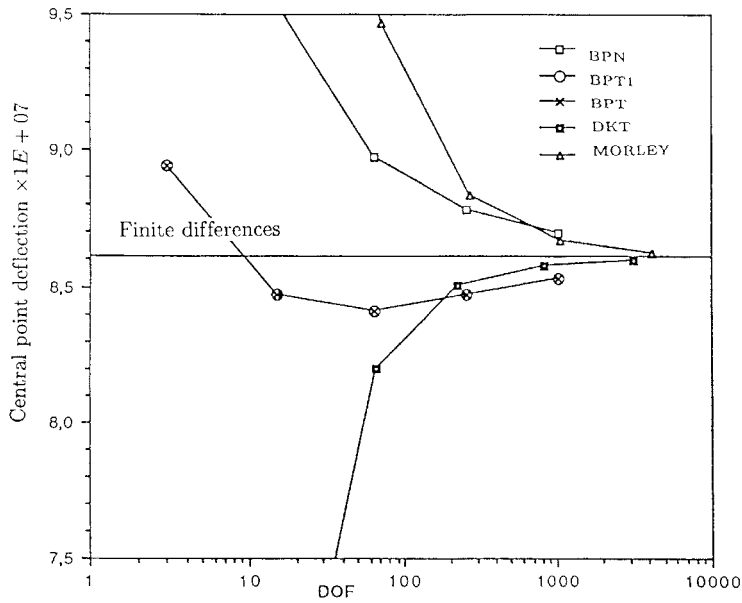

Figure 20. Bi-clamped 30° skewed plate under uniform load. Convergence of central deflection

meshes is shown in the same figure. The results obtained with the new rotation-free BST and BSN triangles compare favourably with those obtained with the DKT-15 [7, 16] element. Further results for this problem using non-structured meshes can be found in [38].

Open spherical dome under opposite diametral point loads

The geometry of the dome, the material properties and the mesh is shown in Figure 27. Again the solution reported here has been obtained using structured meshes. A non-structured mesh analysis can be found in [38].
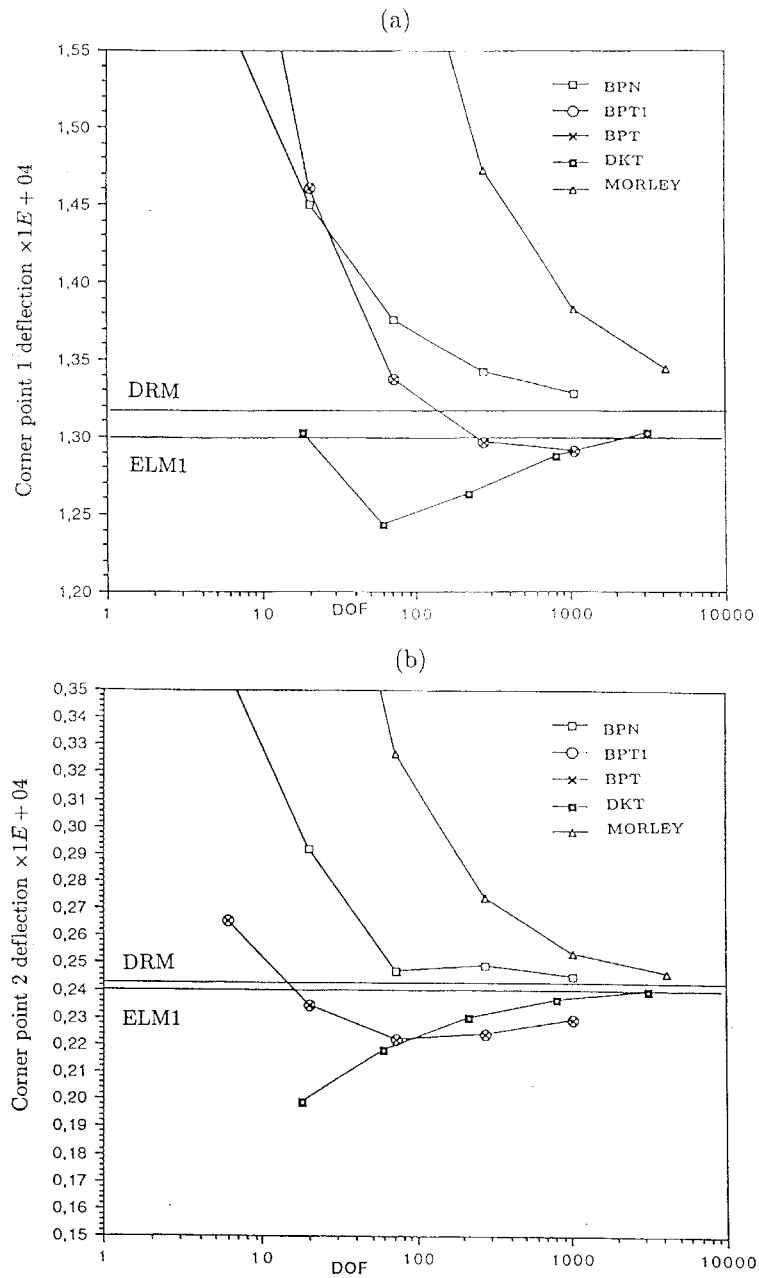
Figure 21. 60° skew cantilever plate under uniform load: (a) Convergence of deflection of corner point 1; (b) convergence of deflection of corner point 2
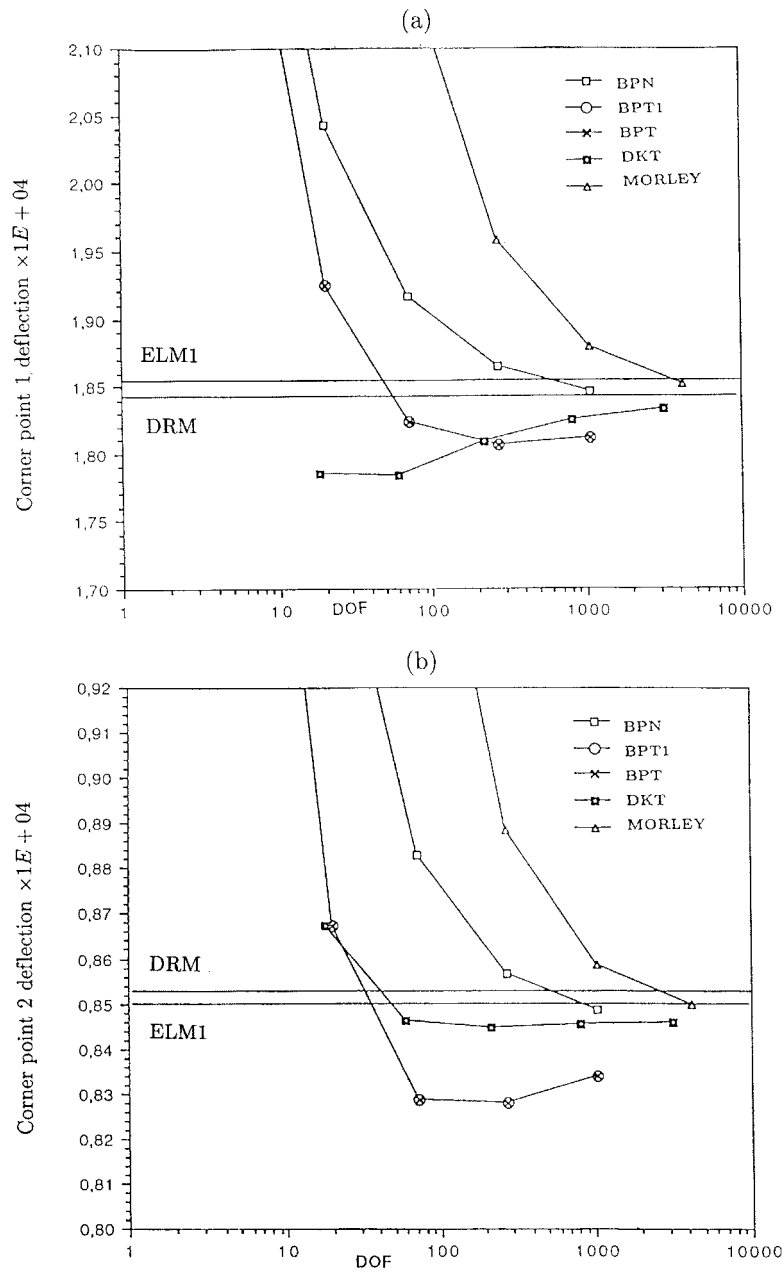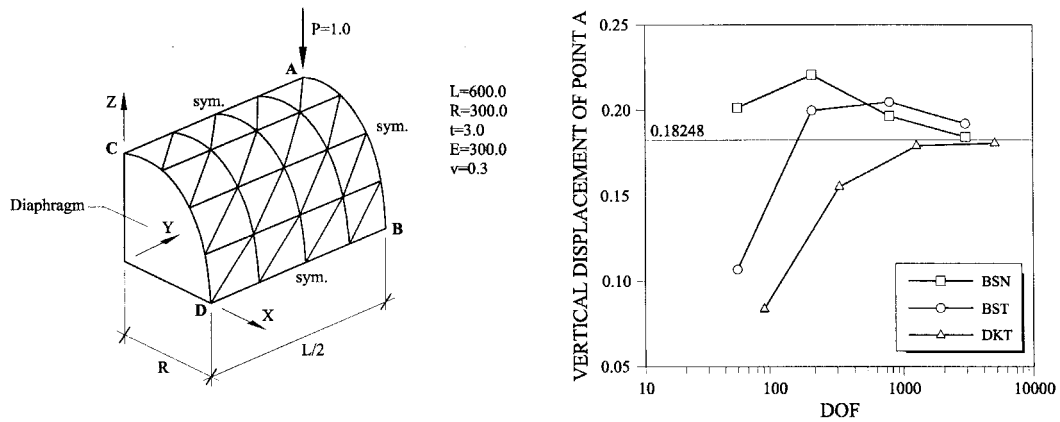
Figure 22. 40° skew cantilever plate under uniform load: (a) Convergence of deflection of corner point 1; (b) convergence of deflection of corner point 2

Int. J. Numer. Meth. Engng. **47**, 557–603 (2000)
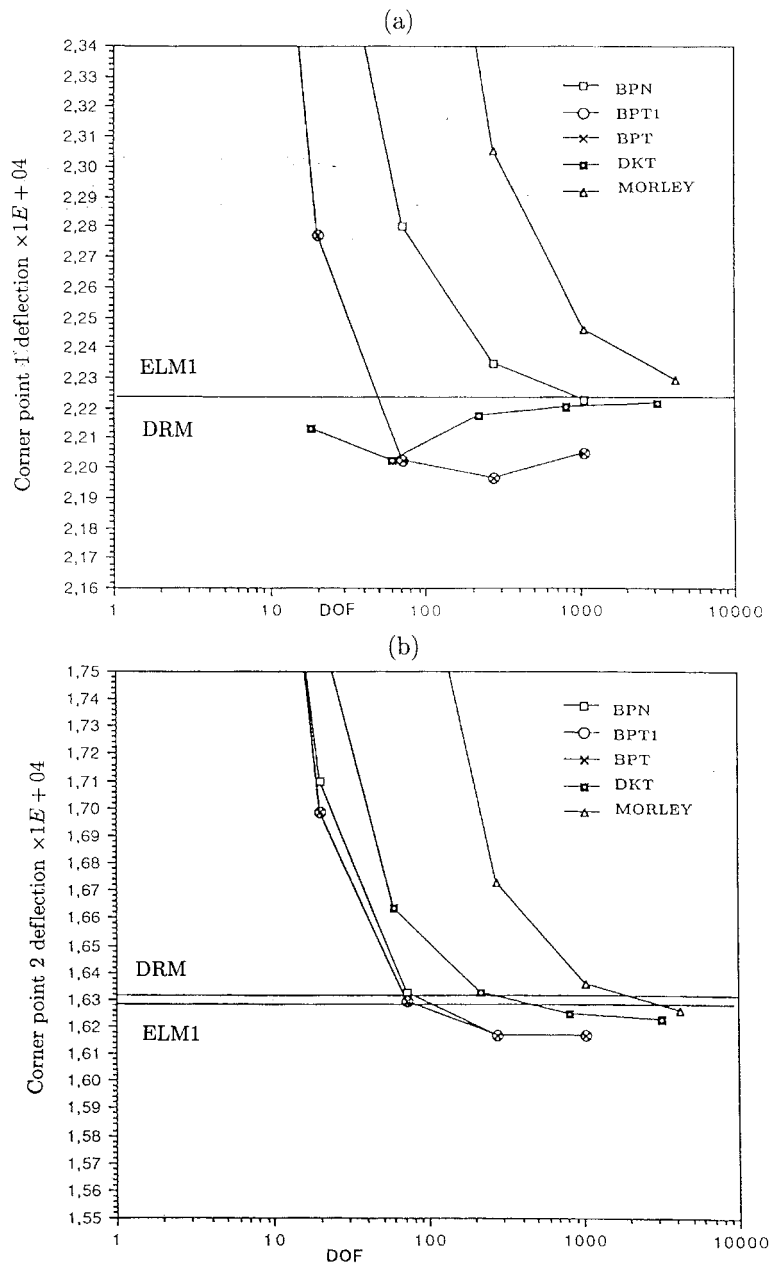
Figure 23. 20° skew cantilever plate under uniform load: (a) Convergence of deflection of corner point 1; (b) convergence of deflection of corner point 2

Figure 24. Cylindrical shell under central point load. Error in vertical displacement of point *A* for different structured meshes of BST, BSN and DKT-15 elements
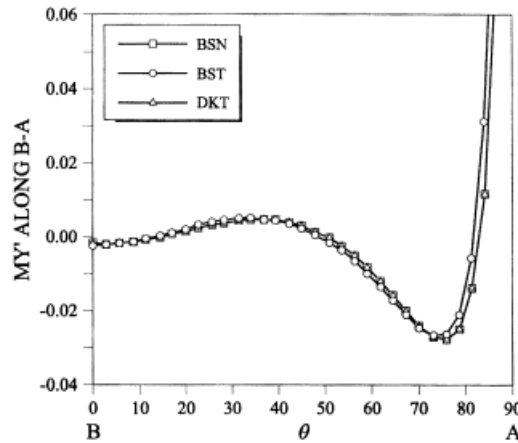
Figure 25. Cylindrical shell under point load. Distribution of M_{y1} bending moment along side B-A for BST, BSN and DKT-15 elements

Figure 27 shows the convergence for the radial displacement of point *A* obtained with the BPT, BSN and DKT-15 elements. Numerical results converge in all cases to a stiffer solution than the reference value of 0·093 [11, 43]. This well-known defect is due to the appearance of strain energy causing an over stiff flexural response commonly known as membrane locking [44]. Methods to elliminate this defficiency are presented in [8].
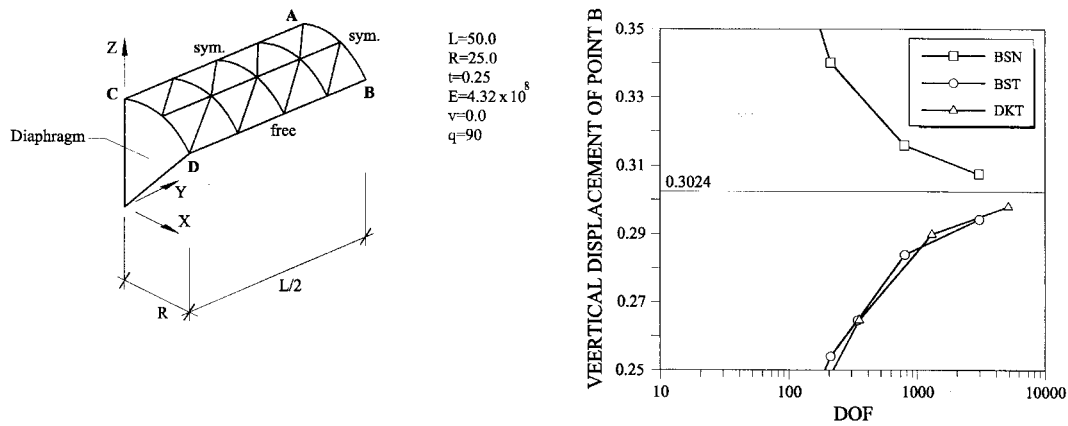
Figure 26. Cylindrical shell under uniform load. Convergence of vertical displacement of point *B* for different structured meshes of BST, BSN and DKT-15 elements
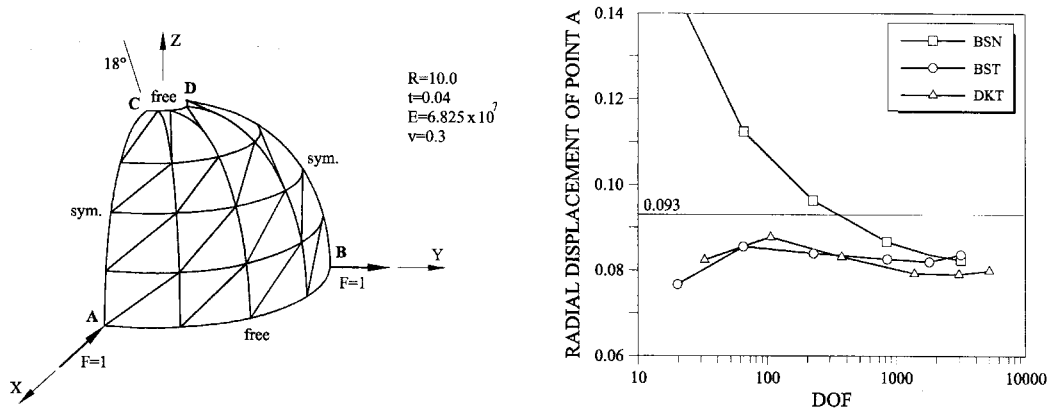

Figure 27. Open spherical dome under point load. Error in radial displacement of point *A* for different structured meshes of BST, BSN and DKT-15 elements

Table I. Open spherical dome. Radial displacement of point *A* obtained with a structured mesh of 2048 triangles using BST, BSN and DKT-15 elements

| | | Rotation-free shell triangles | | | | DKT-15 | | | |
| | | BST | | BSN | | | | | |
No. of triangles	d.o.f	w_A	Error	w_A	Error	No. of triangles	d.o.f.	w_A	error
2048	3200	0·0835	10·2 Per cent	0·0821	11·7	2048	5312	0·0798	14·2 Per cent

Some numerical results are shown in Table I. Note that the behaviour of the BST and BSN elements is more accurate than the DKT-15 element for a considerably smaller number of degrees of freedom.
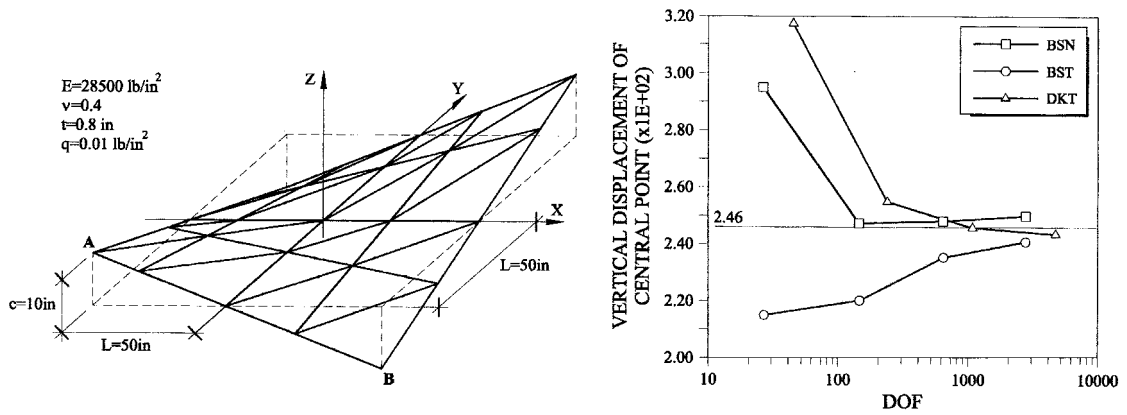
Figure 28. Hyperbolic shell under uniform load. Convergence of vertical displacement of central point for different structured meshes of BST, BSN and DKT-15 elements
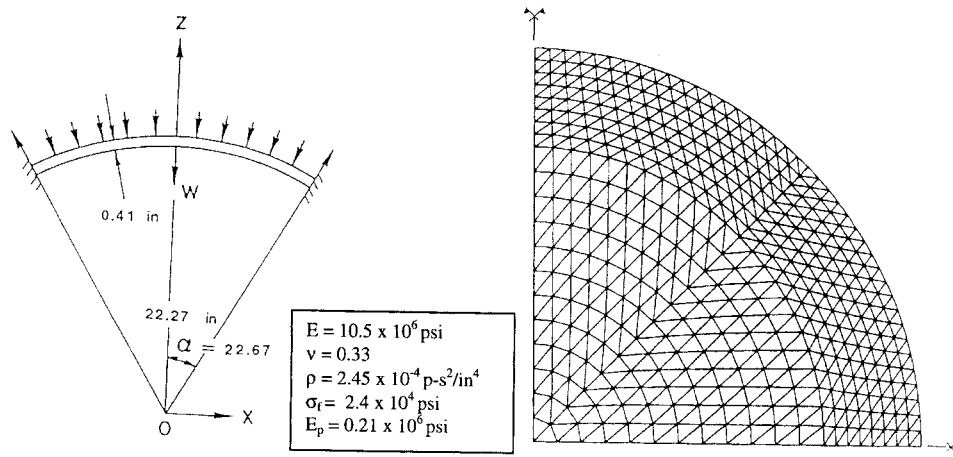
Figure 29. Spherical cup under uniform impulse loading. Geometry, material properties and triangular mesh for analysis with BST, BSN and DKT elements

Hyperbolic shell under uniform load

The geometry of the shell and the material properties are shown in Figure 28. A comparison of the central deflection values obtained with different structured meshes using BST, BSN and DKT-15 elements is shown in Figure 28 where a reference solution is also shown [45]. Note the accuracy of less than $\simeq 10$ per cent error obtained in all cases for meshes with more than 100 d.o.f.

Spherical cap under uniform impulse loading

The last example shows the efficiency of the new BST and BSN rotation-free shell triangles for explicit dynamic analysis of shell structures.
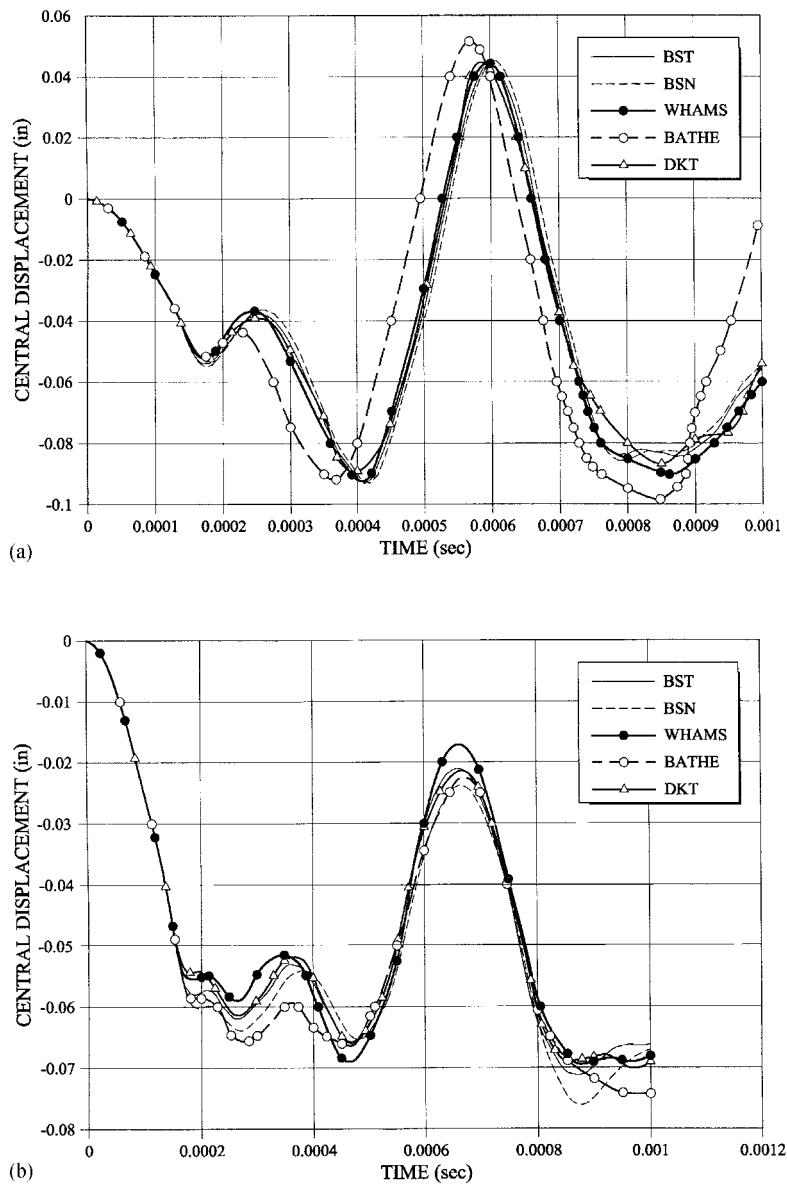
Figure 30. (a) Spherical cup under uniform impulse loading. Evolution of central displacement; elastic solution; (b) Elastoplastic solution. Results obtained with BST, BSN, and DKT elements are compared with those obtained by Bathe [48] and using the explicit dynamic code WHAMS [47]

The problem description and the mesh of 800 triangles (1082 d.o.f.) used to discretize the spherical cap are shown in Figure 29. Fourfold symmetry was used. A uniform load of 600 psi was applied over the cap as shown. Both elastic and elasto-plastic materials with the material properties given in Figure 28 were considered. The results for the central deflection obtained with

the BST and BSN elements are compared in Figures 30(a) and 30(b) to those obtained with the DKT-15 element [46] and with results reported in references [47, 48]. Note the accuracy of the new rotation-free triangles for both the linear and non-linear solutions.

Other examples of the performance of the new rotation-free shell triangles for non-linear dynamic analysis problems including frictional contact conditions are reported in [49–52].

CONCLUDING REMARKS

A general methodology for deriving rotation-free plate and shell triangles has been described. The two element families here presented result from combining cell centred and cell vertex finite volume schemes with finite element interpolations over triangular elements. The simplest elements of these two families, i.e. those corresponding to a linear displacement interpolation, have been described in some detail. The resulting plate and shell triangles are simple and inexpensive as they only involve translational degrees of freedom as nodal variables.

The performace of the new rotation-free plate and shell triangles has been found to be very good in all cases studied. The elements seen particularly promising for competitive analysis of large-scale non-linear shell problems typical of sheet metal forming and crash-worthiness situations.

REFERENCES

1. Zienkiewicz OC, Taylor RC., *The finite element method* (4th edn), vol. 1. McGraw Hill: New York, 1989.
2. Stolarski H, Belytschko T, Lee S-H. A review of shell finite elements and corotational theories. *Computational Mechanics Advances*, 1995; **2**(2):125–212.
3. Idelsohn S, Oñate E, Dvorkin EN (eds), Proceedings of IACM IV World Congress on Computational Mechanics, CIMNE, Barcelona, 1998.
4. Timoshenko SP. *Theory of Plates and Shells*. McGraw Hill: New York, 1979.
5. Dvorkin EN, Bathe KJ. A continuum mechanics based four node shell element for general non-linear analysis. *Engineering Computations*, 1984; **1**:77–88.
6. Morley LSD. On the constant moment plate bending element. *Journal of Strain Analysis* 1971; **6**:10–14.
7. Batoz JL, Bathe KJ, Ho LW. A study of three-node triangular plate bending elements. *International Journal for Numerical Methods in Engineering* 1980; **15**:1771–1812.
8. Carpenter N, Stolarski H, Belytschko T. Improvements in 3-node triangular shell elements. *International Journal for Numerical Methods in Engineering* 1986; **23**:1643–47.
9. Papadopoulos P, Taylor RL. A triangular element based on Reissner-Mindlin plate theory. *International Journal for Numerical Methods in Engineering* 1988; **30**:1029–49.
10. Batoz JL, Lardeur P. A discrete shear triangular nine d.o.f. element for the analysis of thick to very thin plates. *International Journal for Numerical Methods in Engineering* 1989; **29**:1595–1638.
11. Simó, JC, Fox DD, Rifai MS. On a stress resultant geometrically exact shell model, Part II: The linear theory: computational aspects. *Computer Methods in Applied Mechnics and Engineering*, 1989; **73**:553–592.
12. Zienkiewicz OC, Taylor RL, Papadopoulos P, Oñate E. Plate bending element with discrete constraints: new triangular elements. *Computer and Structures* 1990; **35**:505–522.
13. Auricchio F, Taylor RL. 3 node triangular elements based on Reissner-Mindlin plate theory, Report no. UCB/SEMM-91/04 Dept. Civil Engng. University of California, Berkeley, 1991.
14. Oñate E, Zienkiewicz OC, Suarez B, Taylor RL. A methodology for deriving shear constrained Reissner–Mindlin plate elements. *International Journal for Numerical Methods in Engineering* 1992; **33**:345–367.
15. Batoz JL, Katili I. On a simple triangular Reissner-Mindlin plate element based on incompatible modes and discrete constraints. *International Journal for Numerical Methods in Engineering* 1992; **26**:1603–1632.
16. Batoz JL, *Modèllisation des structures par èlèments fins*. Vol. 3 coques, Hermes: Paris, 1992.
17. Katili I. A new discrete Kirchhoff-Mindlin element based on Mindlin–Reissner plate theory and assumed shear fields. Part I: An extended DKT element for thick plate bending analysis. *International Journal for Numerical Methods in Engineering* 1993; **36**:1859–1883.
18. Zienkiewicz OC, Xu Z, Zeng LF, Samuelsson A, Wiberg NE. Linked interpolation for Reissner-Mindlin plate elements. Part I: A simple quadrilateral. *International Journal for Numerical Methods in Engineering* 1993; **36**:3043–3056.

19. Taylor RL, Auricchio F. Linked interpolation for Reissner–Mindlin plate elements. Part II: A simple triangle. *International Journal for Numerical Methods in Engineering* 1993; **36**:3057–3066.
20. Auricchio F, Taylor RL. A triangular thick plate finite element with an exact thin limit. *Finite Elements in Analysis and Design* 1995; **19**:57–68.
21. Van Keulen F, Bont A, Ernst LJ. Non linear thin shell analysis using a curved triangular element. *Computer Methods in Applied Mechanics and Engineering* 1993; **103**:315–343.
22. Oñate E. A review of some finite element families for thick and thin plate and shell analysis. In: *Recent development in finite element analysis*, Hughes TJR, Oñate E, Zienkiewicz OC (eds), CIMNE, Barcelona, 1999.
23. Oñate E, Zárate F, Flores F. A simple triangular element for thick and thin plate and shell analysis. *International Journal for Numerical Methods in Engineering* 1994; **37**:2569–2582.
24. Uguraz AC. *Stresses in Plates and Shells.* McGraw Hill: New York, 1981.
25. Nay RA, Utku S. An alternative to the finite element method. *Variational Methods Engineering*, 1972; **1**.
26. Barnes MR. Form finding and analysis of tension space structure by dynamic relaxation. *PhD Thesis*, Department of Civil Engineering, The City University, London, 1977.
27. Hampshire JK, Topping BHV, Chan HC. Three node triangular elements with one degree of freedom per node. *Engineering Computations* 1992; **9**:49–62.
28. Phaal R, Calladine CR. A simple class of finite elements for plate and shell problems. I: Elements for beams and thin plates. *International Journal for Numerical Methods in Engineering* 1992; **35**:955–977.
29. Phaal R, Calladine CR. A simple class of finite elements for plate and shell problems. II: An element for thin shells with only translational degrees of freedom. *International Journal for Numerical Methods in Engineering* 1992; **35**:979–996.
30. Yang DY, Jung DW, Song LS, Yoo DJ, Lee JH. Comparative investigation into implicit, explicit and iterative implicit/explicit schemes for simulation of sheet metal forming processes. In: *NUMISHEET'93*, Makinouchi A, Nakamachi E, Oñate E, Wagoner RH (eds), RIKEN: Tokyo 1993; 35–42.
31. Brunet M, Sabourin F. Prediction of necking and wrinkles with a simplified shell element in sheet forming. In Proceedings of the International Conference of Metal Forming Simulation in Industry, II, Kröplin B (Ed.), 27–48, 1994.
32. Rio G, Tathi B, Laurent H. A new efficient finite element model of shell with only three degrees of freedom per node. Applications to industrial deep drawing test. In Recent Developments in Sheet Metal Forming Technology, Barata Marques MJM (ed.), 18th IDDRG Biennial Congress, Lisbon, 1994.
33. Oñate E, Cervera M. Derivation of thin plate bending elements with one degree of freedom per node. *Engineering Computations* 1993; **10**:543–561.
34. Oñate E, Cervera M, Zienkiewicz OC. A finite volume format for structural mechanics. *International Journal for Numerical Methods in Engineering* 1994; **37**:181–201.
35. Zienkiewicz OC, Oñate E. Finite elements versus finite volumes. Is there really a choice? In *Nonlinear Computation Mechanics. State of the Art* Wriggers P, Wagner W (eds), Springer: Berlin, 1991.
36. Idelsohn S, Oñate E. Finite volumes and finite elements: two 'good friends'. *International Journal for Numerical Methods in Engineering* 1994; **37**:3323–3341.
37. Oñate E, Idelsohn S, Zienkiewicz OC, Taylor L. A finite point method in computational mechanics. Applications to convective transport and fluid flow. *International Journal for Numerical Methods in Engineering* 1996; **39**:3 839–3866.
38. Zárate F. New finite elements for plate and shell analysis (in Spanish), *PhD Thesis*, University Politècnica de Catalunya, Barcelona, 1996.
39. Razzaque A. A program for triangular bending elements with derivative smoothing. *International Journal for Numerical Methods in Engineering* 1973; **6**:333–343.
40. Flüge W. *Stress in shells.* Springer: Berlin, 1960.
41. Lindberg GM, Olson MD, Cowper GR. New developments in the finite element analysis of shells, *Quaterly Bulletin*, Vol. 4, Division of Mechanical Engineering and National Aeronautical Establishment, National Research Council of Canada, 1969.
42. Scordelis AC, Lo KS. Computer analysis of cylindrical shells. *Journal of American Concrete Institute* 1969; **61**: 539–561.
43. MacNeal RH, Harder RL. A proposed standard set of problems to test finite element accuracy. *Computer and Structures* 1985; **20**:121–128.
44. Belytschko T, Liu WK, Lam D. Implementation and application of a 9-node Lagrangian shell element with spurios mode control. *Computers and Structures* 1985; **20**:121–128.
45. Connor JJ, Brebia C, Stiffness matrix for shallow rectangular shell elements. *Journal of Engineering Mechanics.*, Divison ASCE, 1967; **93**: 43–45.
46. Cendoya P, Explicit dynamic analysis of shells using rotational dof-free triangles. *PhD Thesis* (in Spanish), UPC, Barcelona, 1996.
47. Bathe KJ, Ramm E, Wilson EL. Finite element formulation for large deformation dynamic analysis. *International Journal for Numerical Methods in Engineering* 1975; **9**:353–386.

48. WHAMS-3D, An Explicit 3D finite element program. KBS2 Inc: Willow Springs, IL 60480, USA.
49. Oñate E, Cendoya P, Rojek J, Miquel J. A simple thin shell triangle with translational degrees of freedom for sheet stamping analysis. *Proceedings of the 3rd International Conference on Numerical Simulation of 3D Sheet Forming Processes* (*NUMISHEET'96*), Dearbon, Michigan, USA, 29 Sept.–3 Oct., 1996.
50. Oñate E, Cendoya P, Rojek J, Miquel J. Non linear explicit dynamic analysis of shell structures using a simple triangle with translational degrees of freedom only. *Proceedings of the International Conference on Computational Engineering Science* (*ICES'97*), San Jose, Costa Rica, May 4–9, 1996.
51. Duffet GA, Oñate E, Rojek J, Zárate F. Stampar: A parallel processing approach to sheet stamping simulations. In Computational Plasticity V, Owen DRJ, Oñate E, Hinton E (eds), CIMNE, Barcelona, 1997.
52. Jovicevic J, Oñate E. Analysis of beams and shells using a rotation-free finite element–finite volume formulation. Monograph CIMNE, Barcelona, 1999.